Evaluating the realism of double moment parameterised particle size distributions in a midlatitude frontal ice cloud with complex microphysics

Article

Published Version

Mammatt, R. M. ORCID: https://orcid.org/0009-0003-9712-6151, Westbrook, C. D. ORCID: https://orcid.org/0000-0002-2889-8815, Crosier, J. and McCusker, K. ORCID: https://orcid.org/0000-0002-1886-5323 (2026) Evaluating the realism of double moment parameterised particle size distributions in a midlatitude frontal ice cloud with complex microphysics. Quarterly Journal of the Royal Meteorological Society. e70172. ISSN 1477-870X doi: 10.1002/qj.70172 Available at https://centaur.reading.ac.uk/129074/

To link to this article DOI: http://dx.doi.org/10.1002/qj.70172

Publisher: Wiley

Received: 30 July 2025 | Revised: 15 January 2026 | Accepted: 24 February 2026

DOI: 10.1002/qj.70172

Quarterly Journal of the Royal Meteorological Society RMetS

RESEARCH ARTICLE

Evaluating the realism of double moment parameterised particle size distributions in a midlatitude frontal ice cloud with complex microphysics

Rosie M. Mammatt[1] | **Christopher D. Westbrook**[1] | **Jonathan Crosier**[2,3] | **Karina McCusker**[1]

[1] Department of Meteorology, University of Reading, Reading, UK

[2] Centre for Atmospheric Science, Department of Earth and Environmental Sciences, University of Manchester, Manchester, UK

[3] National Centre for Atmospheric Science, University of Manchester, Manchester, UK

Correspondence
Rosie M. Mammatt, Department of Meteorology, University of Reading, Reading, UK.
Email: r.m.mammatt@pgr.reading.ac.uk

Funding information
University of Reading Department of Meteorology PhD Scholarship

Abstract

Uncertainties in the representation of ice particle size distributions (PSDs) cause inaccuracies in simulations of clouds, which have negative impacts on weather forecast and climate predictions. In this study, a midlatitude frontal case study from the Parameterizing Ice Cloud using Airborne obServationS and triple frequency dOppler radar (PICASSO) field campaign in the UK is analysed. The cloud was up to 6 km deep and persisted for several hours, which allowed ice PSDs at a range of temperatures from −28°C to near 0°C to be sampled by the Facility for Airborne Atmospheric Measurements (FAAM) research aircraft; this allowed information about a range of microphysical regimes to be captured. We compare observed PSDs and gamma PSDs with the same concentration and ice water content. We find that at low temperatures a gamma distribution is an appropriate fit to the observations, predicting PSDs similar to those observed. However, in warmer, microphysically complex regions with multiple ice crystal habits, some of which may be caused by secondary ice production, a single gamma distribution does not provide an accurate parameterisation of the observed PSDs. We explore the impact of these discrepancies on the microphysical evolution of the cloud by computing the corresponding process rates using the observed and parameterised PSDs. Errors of more than 100% in aggregation rate, around 50% in precipitation and vapour growth rates, and more than 10 dB in radar reflectivity are calculated.

KEYWORDS

ice cloud microphysics, ice particle size distributions, observations

1 | INTRODUCTION

A greater understanding of ice clouds is essential to our comprehension of Earth's weather and climate system. Precipitation timing and intensity, cloud lifetime, radiative balance, and subsequent weather effects are directly affected by ice microphysics. It is therefore vital to represent these microphysical processes accurately in

---

numerical weather prediction (NWP) models. Accurate forecasts are important to a range of users, from the casual weather observer up to the industry scale, which motivates continuous improvement of our understanding of the underpinning processes that control these outcomes. Field and Heymsfield (2015) demonstrate the importance of snow to global precipitation, as a large proportion of precipitation events begin as snow, even in the warmest areas. Clouds also produce some of the greatest uncertainties in future climate predictions (Lohmann & Feichter, 2005; Mülmenstädt *et al.*, 2021; Sherwood *et al.*, 2020). Pasquier *et al.* (2023) present evidence showing that different shapes of ice crystal have different radiative properties, whilst Zhang *et al.* (2022) show evidence that the accuracy of particle size distribution (PSD) shape parameters has a significant impact on climate simulations, especially with respect to long wave cloud radiative effects and convective precipitation rates.

Operational NWP models are largely still reliant on single moment microphysics schemes (Lean *et al.*, 2008; Senior & Mitchell, 1993; Wilson & Ballard, 1999), despite the evidence that they do not represent some precipitation processes sufficiently (Bryan & Morrison, 2012; Milbrandt & Yau, 2005). Whereas climate models have opted to use double moment microphysics schemes operationally, motivated by improved aerosol–cloud interactions (Lohmann *et al.*, 2007; Morrison & Gettelman, 2008), the adoption of double moment schemes in weather prediction is a relatively recent development. An example of this is the Cloud AeroSol Interacting Microphysics (CASIM) scheme, which is the next generation double moment microphysical scheme for the UK Met Office model (Field *et al.*, 2023). CASIM prognoses a mass mixing ratio proportional to the ice water content (IWC) and a number concentration of particles for three ice species (cloud ice, snow, and graupel) and represents PSDs using a gamma distribution. As cloud ice autoconverts rapidly to snow at sizes greater than 100 μm, and there is no observed graupel in our case study, we are therefore interested in the snow category in CASIM for the analysis that follows.

Marshall and Palmer (1948) studied ground observations of raindrops on dyed filter papers and concluded that the size distribution of natural raindrops followed an exponential form. Gunn and Marshall (1958) undertook a similar investigation with snowflakes. From their observations, they deduced that natural snowflakes also follow an exponential distribution. Since then, ice PSDs have been represented in this relatively simplistic way in models (Lin *et al.*, 1983; Reisner *et al.*, 1998; Sekhon & Srivastava, 1970; Wilson & Ballard, 1999) and remote sensing retrievals (Billault-Roux *et al.*, 2023b; Kneifel *et al.*, 2011, 2015). Other studies (Ferrier, 1994; Heymsfield *et al.*, 2013; Milbrandt & McTaggart-Cowan, 2010) show evidence that a gamma distribution represents the observed PSD in clouds more accurately. Accurate modelling of natural ice PSDs is essential in NWP and climate models, as inaccuracies can lead to large errors. For example, Wang *et al.* (2020) show evidence that a 33% reduction in ice crystal effective radius uncertainty would lead to a decrease of 60% in the uncertainty in climate sensitivity (the response of global temperature to a doubling in atmospheric carbon dioxide concentration relative to pre-industrial levels) and mean state uncertainty.

For decades, it has been observed that the number of ice particles in clouds can be many times higher than the observed number of ice nuclei (Field *et al.*, 2017). As a result, secondary ice production (SIP) has been a topic of much discussion for many years. Korolev and Leisner (2020) detail the experimental effort that has been put into investigating ice multiplication processes. They define six SIP mechanisms: droplet fragmentation, thermal shock, rime splintering, sublimation fragmentation, ice–ice collisions, and ice nucleating particle (INP) activation. Considerable research effort has been put into investigating the rime splintering and droplet fragmentation processes. Hallett and Mossop (1974) first published evidence for the rime splintering mechanism and, since then, there have been numerous further studies investigating this process (Billault-Roux *et al.*, 2023a; Crosier *et al.*, 2011; Keppas *et al.*, 2017; Lloyd *et al.*, 2014, 2020). However, there are also recent laboratory studies (Seidel *et al.*, 2024) disputing that the rime splintering process is sufficiently effective to cause the mismatch in concentrations between ice nuclei and ice-crystal concentrations that has frequently been observed. Phillips *et al.* (2018), Keinert *et al.* (2020), and Lauber *et al.* (2021) show that there is observational evidence to suggest that drizzle drop fragmentation may be an efficient ice multiplication mechanism initiated by updrafts in natural convective and orographic clouds. There have also been studies showing evidence for collisional ice–ice breakup as an efficient source of secondary ice particles (Phillips *et al.*, 2017; Vardiman, 1978; Yano & Phillips, 2011). In contrast, there have been studies showing evidence that dendrites have a higher aggregation efficiency (Connolly *et al.*, 2012; von Terzi *et al.*, 2022), leading to increasingly large particles instead of the production of smaller particles by collisional breakup. To our knowledge, there is very limited observational evidence on the modification of the PSD shape caused by secondary ice processes in the existing literature. We expect that, for example, rime splintering will introduce large numbers of small ice fragments into a highly ice supersaturated environment, leading to their rapid growth into crystals due to the Bergeron–Findeisen mechanism (e.g., Hogan *et al.*, 2003). If this process occurs with a deeper cloud system, these new crystals are superimposed on a background ice particle population, potentially leading to a multimodal PSD. Other secondary ice processes, such as ice–ice collisional breakup, are also expected to increase the concentration of smaller particles, changing the shape of the PSD.

In this study, observations from a midlatitude frontal ice cloud are examined to understand the microphysical characteristics that determine PSD shape better. We evaluate how well the observed PSDs match the parameterised PSD from the UK Met Office's next generation double moment microphysics scheme CASIM (Field *et al.*, 2023). This cloud is microphysically complex at lower levels, and in a number of runs we observed multiple particle habits coexisting in the same volume. We argue that some of these runs may have been influenced by SIP and we investigate the impact that these secondary particles have on the PSD shape and its deviation from the parameterised distributions. We highlight the importance of this work by computing vapour growth, precipitation and aggregation rates, and radar reflectivity from the observed and parameterised distributions to demonstrate the inaccuracies that can arise as a result of using a single gamma distribution to represent ice PSDs.

2 | DATASET AND INSTRUMENTATION

2.1 | In situ measurements

Our analysis uses in situ aircraft data from the National Centre for Atmospheric Science (NCAS) managed Facility for Airborne Atmospheric Measurements (FAAM) aircraft. The data were collected during the Parameterizing Ice Clouds using Airborne obServationS and triple-frequency dOppler radar data (PICASSO) field campaign, which was carried out in the vicinity of the Chilbolton Facility for Atmospheric and Radio Research (CFARR), Southern England, in 2018–2019. During the campaign, the FAAM aircraft performed straight and level runs (SLR, hereafter referred to as runs) and collected data on a range of meteorological variables. The most important variable in this study is the measured PSD, which is measured using several optical array probes (OAPs). For the PICASSO campaign, the aircraft was equipped with a Two-Dimensional Spectrometer (2DS) probe (Lawson *et al.*, 2006), a High Volume Precipitation Spectrometer (HVPS) probe (Lawson *et al.*, 1998), two Cloud Imaging Probes (CIPs: Baumgardner *et al.*, 2001), which differ in the maximum particle size they can measure, a Cloud Particle Imager (CPI: Lawson *et al.*, 2001), and a Cloud Droplet Probe (CDP: Lance *et al.*, 2010). The main properties of these probes, their principles of operation, and observable particle size ranges are summarised in Table 1.

To characterise the ice particle size distributions in this study, we use measurements from the HVPS probe. This probe has the largest sample volume of the instrument suite and therefore the best sampling statistics, allowing high quality PSD data even at relatively low concentrations and high time resolution. The key disadvantage of this probe is its limited resolution, with a pixel size of 150 μm. This means that the images of submillimetre particles are very coarse, and this could have implications for the accuracy of the PSDs. To verify the HVPS spectra, we have compared them with the PSDs measured by the 2DS probe, which has a much higher resolution of 10 μm. Figure 1 shows this comparison. Note that the 2DS and HVPS probes do not sample the same individual particles, but they sample the same statistical population. The data have been averaged across the full length of

TABLE 1 Summary of key properties of the probes in operation during flight C082.

Type of probe	Probe name	Principle of operation	Size range	Bin width[a]
Optical Array Probes	2DS	Samples the shadows of particles as they pass through a laser beam	10 μm–1280 μm	10 μm
	HVPS-3		150 μm–19.2 mm	150 μm
	CIP-15		15 μm–960 μm	15 μm
	CIP-100		100 μm–6.4 mm	100 μm
High Resolution Imager	CPI	Lasers detect and illuminate a particle, a camera takes a photograph	15 μm–2.5 mm	2.3 μm
Light Scatting Probe	CDP	Detects pulses of light forward scattered by droplets passing through a laser beam	2 μm–50 μm	1–2 μm[b]

[a] The values quoted here are related to the measured size of the particle shadows, which are proxies for particle size. In reality, particles can be larger or smaller than the reported size, depending on the position within the sample volume.

[b] The bin width is 1 μm for particle sizes of 2–11 μm and 2 μm for particle sizes of 12–50 μm.

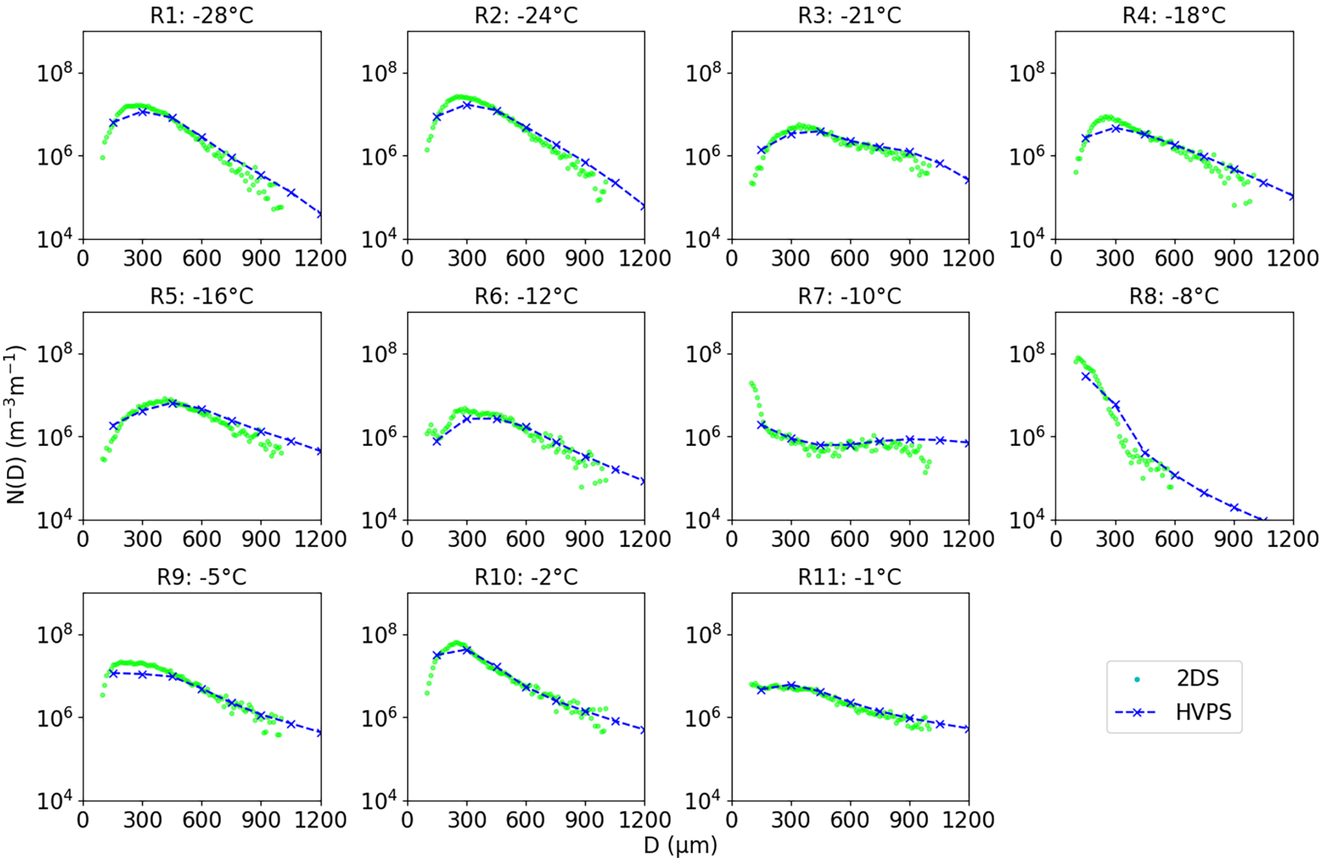

FIGURE 1 Average PSD per run measured by the 2DS probe (points) and the HVPS probe (crosses) at small sizes. Only the sizes covered by the 2DS probe (up to 1280 μm) are shown in this figure, but later figures show HVPS data for a greater range of particle sizes. The run number above each panel corresponds to the runs described in Table 2. From this, we see there that is generally good agreement between the two OAPs at small particle sizes. [Colour figure can be viewed at wileyonlinelibrary.com]

the run to obtain good sampling statistics. The 2DS data have been filtered such that only images classified as ice are included (this is discussed in more detail shortly, in Section 2.3). We find that the two probes are in good agreement in all runs. The coarser size bins of the HVPS smooth out sharp peaks in the PSD (e.g., R4 at 250 μm), but the magnitude and breadth of the distribution appears well captured.

2.2 | Meteorological conditions

On February 14, 2018, the FAAM aircraft flew through a large, frontal ice cloud (flight reference C082). From Figure 2a, we can see that this cloud was associated with a complex, multi-fronted synoptic situation over the UK. The vertical radiosonde profile in Figure 2b shows a saturated air mass, as the temperature and dewpoint temperature are almost identical throughout the ascent and consequently the relative humidity remains high.

Throughout the measurement period, the Copernicus Ka-band radar at CFARR was vertically pointing and therefore capturing the structure of the cloud as it passed over the area, shown in Figure 3a (see Illingworth *et al.*, 2007 for instrument specifications and capabilities). The ice cloud above the melting layer was up to 6 km deep and persisted for several hours, which allowed ice PSDs at a range of temperatures from −28 °C to near 0 °C to be sampled by the FAAM research aircraft; this allowed information about a range of microphysical regimes to be captured. It is clear that the upper levels of the cloud, above around 5 km, are less homogenous than at lower altitudes. This figure shows areas where either there are gaps in the cloud or the reflectivity falls below the minimum detectable reflectivity. This is consistent with the radiosonde profile shown in Figure 2b, which is close to saturation with respect to liquid water below 5 km and increasingly dry above that. The runs that we analyse in this study were chosen so that the aircraft was always “in cloud” and therefore sampling particles at these higher altitudes. Comparison of the radiosonde profile in Figure 2b and the aircraft trace in Figure 3a shows that the aircraft sampled a wide range of microphysical conditions between temperatures of −30 °C and 5 °C. Figure 3b shows that there was continuous rainfall throughout the

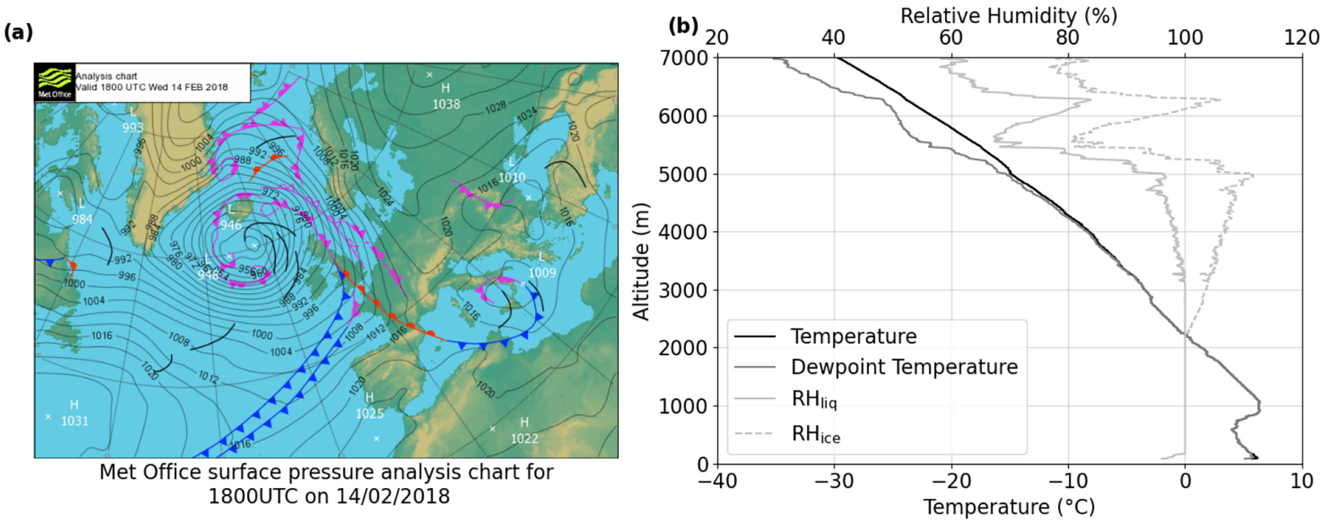

Met Office surface pressure analysis chart for 1800UTC on 14/02/2018

FIGURE 2 (a) Surface pressure analysis chart from the UK Met Office, valid for 1800 UTC on February 14, 2018. (b) Vertical temperature, dewpoint temperature, and relative humidity with respect to liquid and ice from a radiosonde ascent, launched from CFARR at 1900 UTC on February 14, 2018. RH_{ice} was calculated from the measured RH_{liq}. [Colour figure can be viewed at wileyonlinelibrary.com]

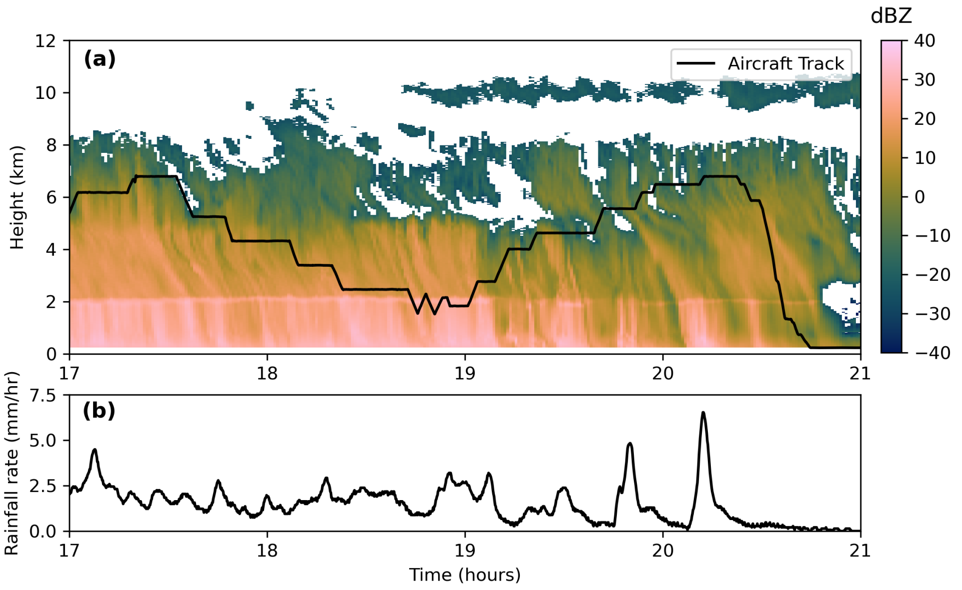

FIGURE 3 (a) Radar reflectivity measured using the Copernicus Ka-band (35 GHz) radar during this case study. The time series of the altitude of the FAAM aircraft is shown in black. The minimum detectable reflectivity of the radar is approximately −25 dBZ at a 10 km range. (b) 100 second moving average of rainfall rate measured by a rain gauge at CFARR. [Colour figure can be viewed at wileyonlinelibrary.com]

measurement period, measured by a high resolution rain gauge at CFARR (Norbury & White, 1971).

Figure 4a shows the movements of the aircraft during the case study; it sampled a line approximately 80 km long between CFARR (51.1145°N, 1.4370°W) and Wardon Hill (50.8193°N, 2.5563°W). The aircraft was not located over CFARR throughout the flight period, but made overpasses on each run. Figure 4b shows the altitude of the aircraft over the course of the flight. Table 2 provides more detail on the scientific runs that are used in this study. They cover a range of altitudes through the cloud and we can therefore see many different microphysical regimes that coexist in this cloud. We study runs between −28 and −1 °C at altitudes between 6.7 and 2.4 km. The ice particle concentration and estimated IWC vary substantially between runs. The lowest ice particle concentration of 0.1 L^{-1} and estimated IWC of 2.0 mgm^{-1} occurred in R6, whilst the highest ice particle concentration of 16.6 L^{-1} and estimated IWC of 74.6 mgm^{-1} were observed in R10.

2.3 | Phase of the sampled hydrometeors

In this subsection, we characterise the phase of the particles present in the cloud. To do this, we have performed a range of inspections and analyses. A simple check is via

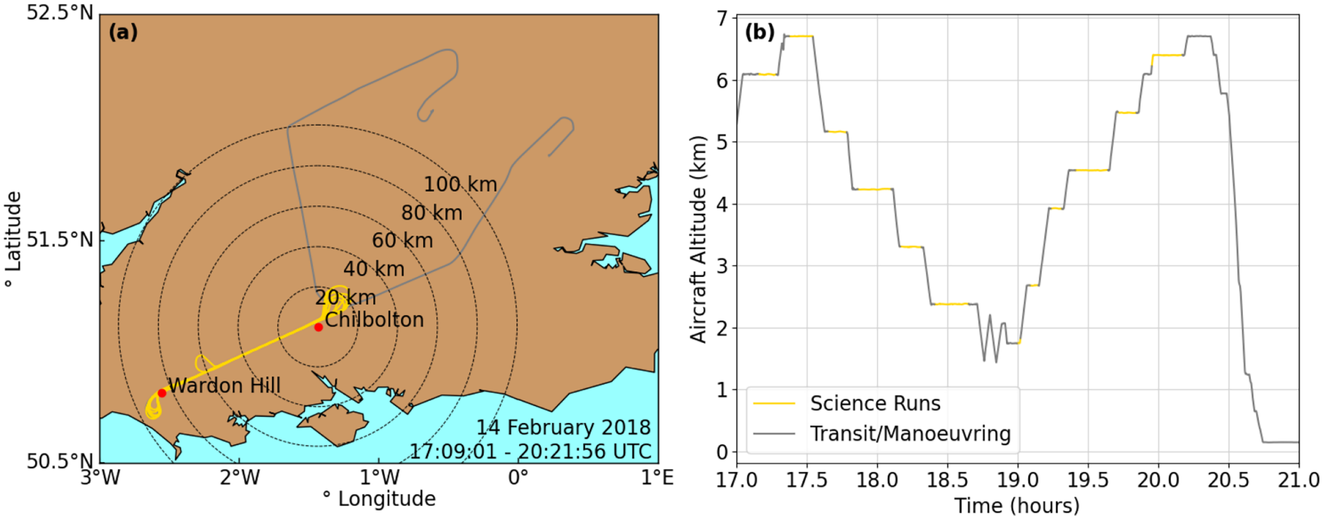

FIGURE 4 Flight track of the aircraft during this case study on February 14, 2018. In both panels, the grey line indicates the aircraft's movement whilst in transit, both to and from takeoff and landing sites and between scientific runs, whilst the yellow lines show where the scientific runs occur. (a) The location over the UK where the flight took place. The locations of the radars at Chilbolton and Wardon Hill are marked. The dashed rings show the distance away from CFARR at 20 km increments. (b) The altitude of the aircraft throughout the flight. [Colour figure can be viewed at wileyonlinelibrary.com]

visual inspection of the HVPS images. This has been done (examples are shown later, in Figures 13–17) and shows a dominance of ice particles throughout all of the runs. However the resolution of the HVPS is coarse (150 μm pixels) and therefore submillimetre particles are only a few pixels wide, making a diagnosis of particle type more difficult. To determine the phase of these smaller particles, we have examined the images from the 2DS probe, which has much finer (10 μm) resolution. A convenient way to classify the shape of these images is by measuring their irregularity, based on the perimeter P and area A of the images, as described in Crosier *et al.* (2011), Taylor *et al.* (2016), and Baumgardner *et al.* (2017). Low irregularity (LI) particles are nearly circular with $P^2/4\pi A \approx 1$ and these particles are therefore very likely to be water drops. High irregularity particles have a larger perimeter for a given area ($P^2/4\pi A > 1.4$), which means a distinctly non-circular image, and are highly likely to be ice particles. Medium irregularity (MI) images lie in between these two categories, and are diagnosed infrequently.

The stacked area plot in Figure 5 shows the percentage of particles in each irregularity category from each 2DS size bin. For reference, the overlaid dashed lines show the edges of the HVPS size bins. We see that, at sizes greater than 250 μm, the data are dominated by ice particles with high irregularity in all runs. Only at smaller sizes is there a significant fraction of low irregularity particles. However, some care is needed in the interpretation of these near-circular images, as it is possible for ice particles to be diagnosed as LI if they are poorly imaged, or if they are small and regular in shape (e.g., short columns or thick plates). Analysis of the data at the coldest temperatures (-28 to -18 °C) gives an indication of the magnitude of this effect. Around a quarter of the particles are classified as LI at $D = 75$ μm in R1 and R2; however, we do not expect significant numbers of supercooled drizzle drops in such cold clouds. The fraction of LI particles as a function of size is very consistent across R1–R6 and R9, which suggests it is not a microphysical characteristic of the cloud (which is expected to be variable in time and space) but instead is a feature of the imaging and classification process. Inspection of images, such as those shown in Figure 6, from the CPI probe in these runs (which has an even finer resolution than the 2DS, but very low sample volume) confirms this view, as no particle in this size range in R1–R6 is a drop. Figure 6a shows examples of particles of 100–200 μm size that are observed in R1. This offers a clear diagnosis that the PSDs in these runs are ice dominated.

In runs R7, R8, R10, and R11 we observe that a larger fraction of particles with $D \sim 100$ μm are classified as LI. This indicates that small drizzle drops are present in these runs, in addition to ice particles. To confirm this, the corresponding CPI imagery was inspected, which indeed reveals the presence of small drops, with drop sizes clustered around 100 μm. An example of these particles from R8 is shown in Figure 6b.

In our verification of the HVPS spectra in Figure 1, we compared the HVPS data with the HI PSDs from the 2DS (i.e. only the ice-phase particles). This confirms that the drizzle drops in this case are too small to influence the HVPS data, and therefore that the PSDs we analyse in what follows represent the ice particles in the cloud, but not the

TABLE 2 Summary of the scientific runs used in this study. Note that the run numbers are based on altitude/temperature, not time. LQ and UQ are the lower and upper quartiles, respectively. The particle habits in **bold** show the most common particle shape, with descending frequency listed sequentially.

Run	Start time (UTC)	End time (UTC)	Temperature[a] (°C)	Altitude (km)	Ice particle concentration (L^{-1})			IWC[b] (mgm^{-3})			Particle Habits
					LQ	Median	UQ	LQ	Median	UQ	
R1	1722:18	1732:32	−28	6.71	1.6	3.6	6.8	3.7	12.2	25.5	**Polycrystals**, plates
R2	1957:16	2010:21	−24	6.33	4.5	6.5	9.0	18.8	28.3	42.0	**Polycrystals**, plates
R3	1709:01	1717:00	−21	6.11	0.6	1.6	3.3	3.1	9.3	22.6	**Polycrystals**, columns, plates
R4	1942:44	1950:45	−18	5.49	0.5	1.4	3.4	4.2	12.3	18.4	**Polycrystals**, plates
R5	1738:50	1747:01	−16	5.19	2.1	2.8	4.2	20.8	30.4	44.8	**Polycrystals**, plates, columns
R6	1924:32	1938:35	−12	4.58	0.01	0.1	2.2	0.2	2.0	20.8	**Polycrystals**, dendrites, drizzle, columns, plates
R7	1751:40	1806:01	−10	4.28	0.7	1.3	2.0	20.6	40.0	70.7	**Dendrites**, polycrystals, aggregates, drizzle, columns, plates
R8	1914:05	1918:54	−8	3.97	0.8	3.5	11.0	1.9	5.8	14.2	**Dendrites**, drizzle, aggregates, columns
R9	1809:46	1819:00	−5	3.36	2.7	5.5	8.9	47.1	65.3	88.6	**Columns**, needles, drizzle, aggregates, dendrites
R10	1905:09	1908:52	−2	2.75	13.1	16.6	18.2	36.6	74.6	99.5	**Needles**, columns, drizzle, aggregates, ice lollies[c], plates
R11	1824:26	1839:07	−1	2.45	2.3	3.1	4.0	23.6	63.0	87.5	**Needles**, columns, aggregates, drizzle, ice lollies,[c] dendrites

[a] The temperature of each run is taken from the radiosonde data (shown in Figure 2b), due to issues with the temperature sensors on the aircraft during this flight.

[b] The IWC shown is estimated from the PSD, using the mass–size relationship of Cotton *et al.* (2013). Here, $\mathrm{IWC} = 0.0257 \int N(D) D^2 \, dD$, where $N(D)$ is the PSD, D is the particle diameter, and dD is the bin width of the OAP.

[c] As described in Keppas *et al.* (2017).

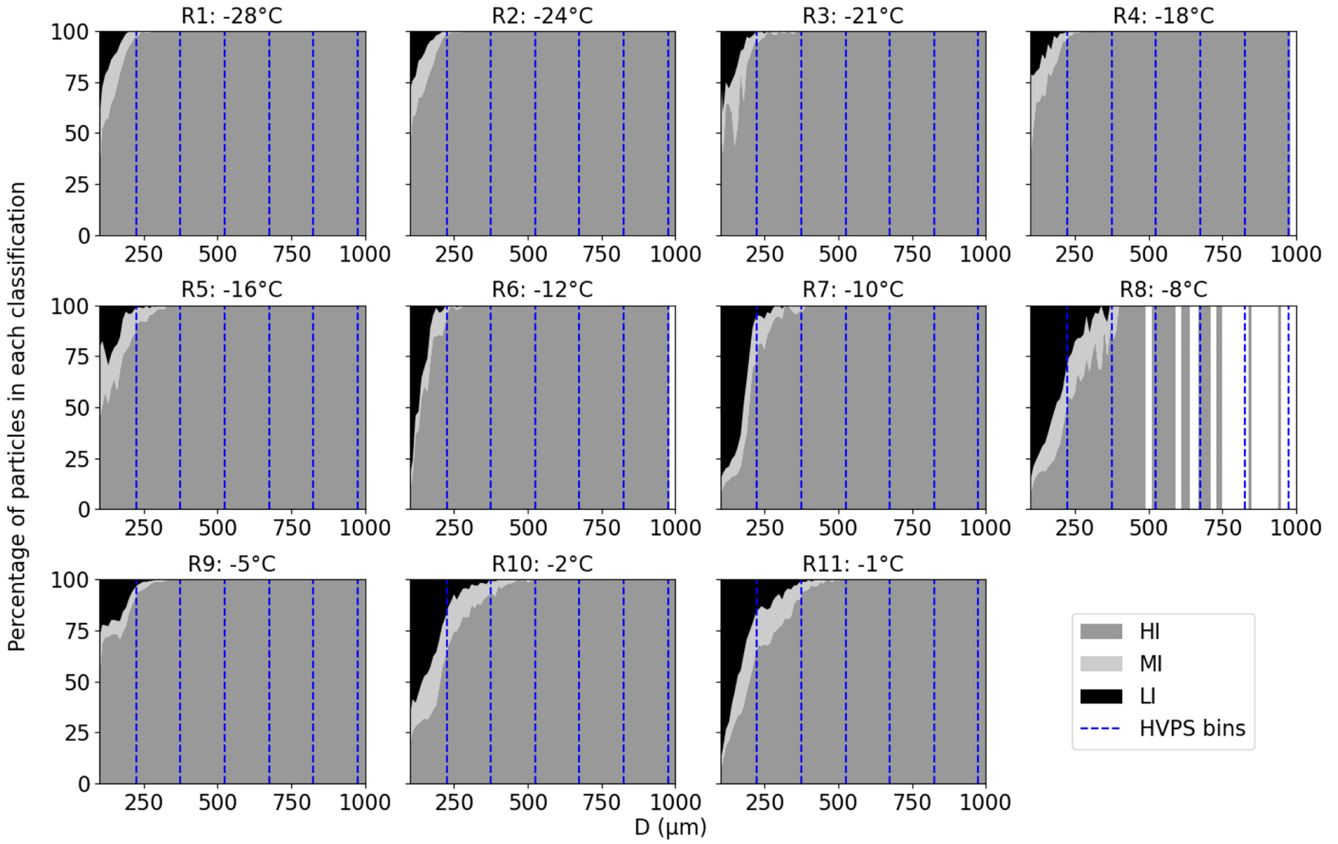

FIGURE 5 The percentage of particles measured by the 2DS probe that are classified as high, medium, or low irregularity in each aircraft run, labelled as HI, MI, and LI. The dashed lines show the edges of each HVPS size bin. From this we can see that, generally, the low irregularity particles are only seen in the first two bins. The run number above each panel corresponds to runs described in Table 2. [Colour figure can be viewed at wileyonlinelibrary.com]

drizzle. In addition to supercooled drizzle drops, some of the runs presented later also contain much smaller cloud droplets with sizes $< 50\ \mu$m. The liquid water content from these cloud droplets is quantified using the CDP probe, and the time series of this quantity is shown in Section 4 as microphysical context; however these droplets are too small to influence the PSDs presented in the analysis that follows.

3 | DOUBLE MOMENT GAMMA DISTRIBUTIONS

In many microphysics schemes, PSDs are represented by gamma distributions in the form

$$N(D) = n_0 D^{\mu} \exp(-\lambda D), \tag{1}$$

where $N(D)$ is the PSD, n_0 is an intercept parameter, D is the particle size, λ is the slope parameter which evolves as mass and number change, and μ is a shape parameter that is fixed in double moment microphysics schemes. To compare the observed PSDs with equivalent gamma distributions, we must define which properties of the observed and gamma PSDs to match. We choose to match the zeroth and second moments of the PSD—more details on this approach are given in Section 3.1.

To link Equation (1) to the observed moments, the intercept parameter n_0 can be expanded to relate to physical quantities:

$$n_0 = n\frac{\lambda^{1+\mu}}{\Gamma(1+\mu)}. \tag{2}$$

Combining Equations (1) and (2) gives a double moment gamma distribution that is directly comparable to observed physical quantities:

$$N(D) = n\frac{\lambda^{1+\mu}}{\Gamma(1+\mu)}D^{\mu} \exp(-\lambda D). \tag{3}$$

It is useful to demonstrate how the different parameters affect the shape of this gamma distribution, which we show in Figure 7. The values of the parameters shown here are chosen to demonstrate the general sensitivity of the gamma distribution to these parameters, and are

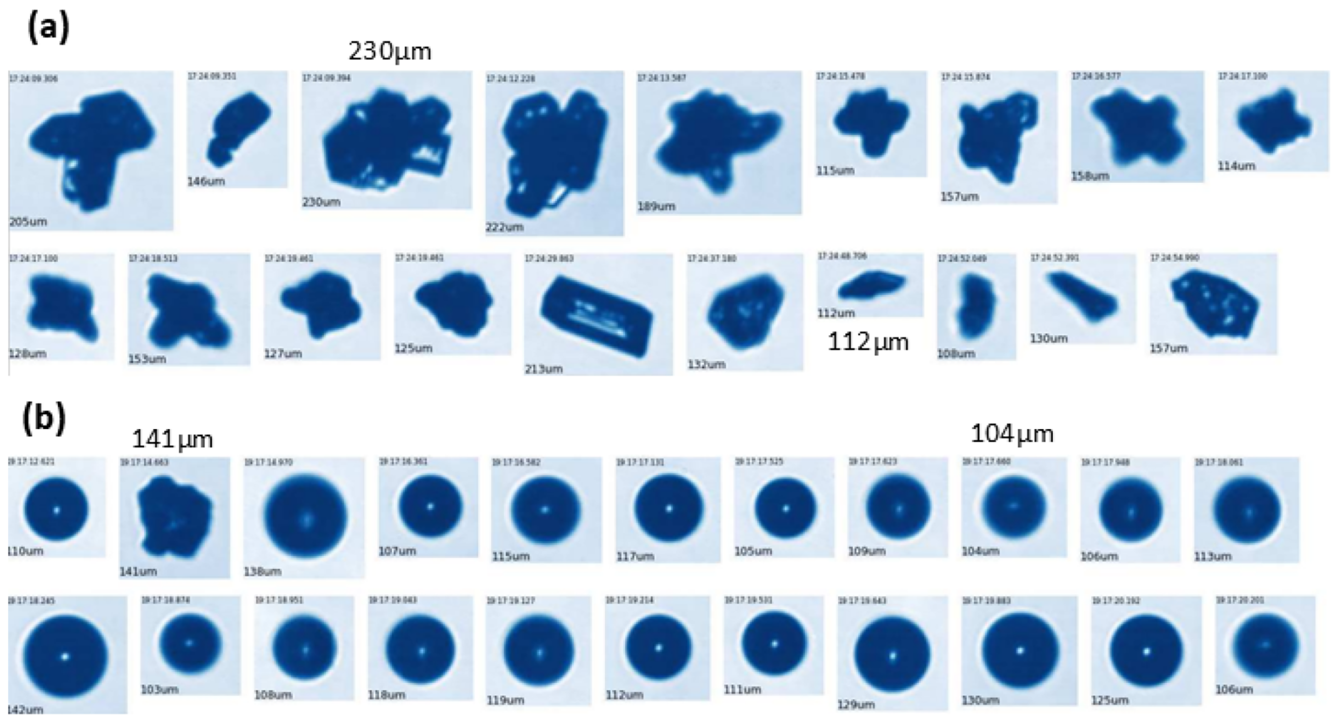

FIGURE 6 Example images from the CPI probe of particles of the order of 100–200 μm in size from (a) R1 and (b) R8, as described in Table 2. The smallest and largest particles from these images have their sizes written adjacently for scale. It is clear from the examples that in R1 these small particles are ice, whereas in R8 these particles are liquid and very consistent in size. [Colour figure can be viewed at wileyonlinelibrary.com]

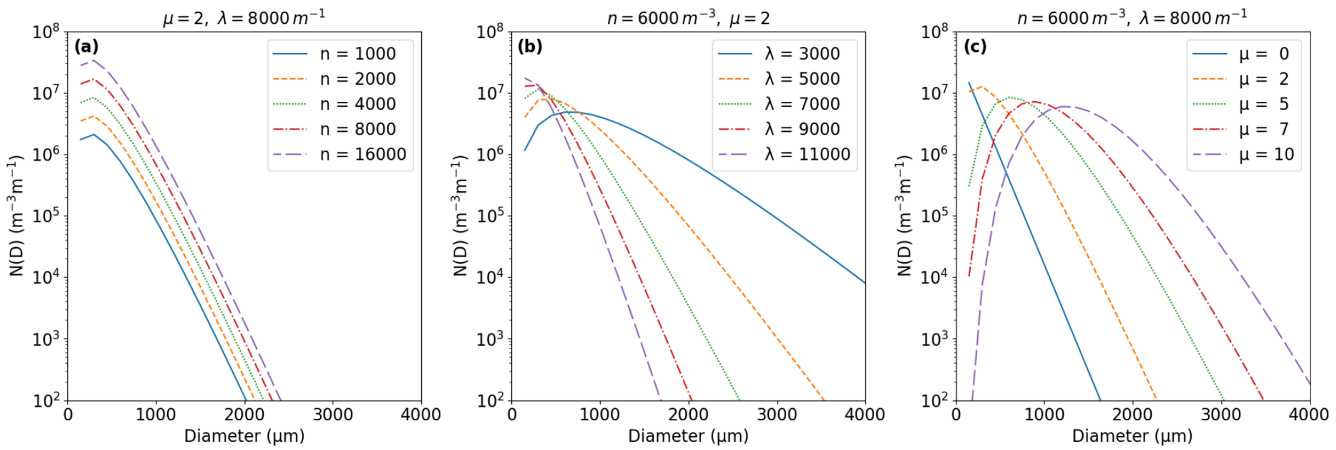

FIGURE 7 This plot demonstrates the effect of changing PSD parameters on the resulting gamma distribution. The gamma distribution used is from Field *et al.* (2023), parameterised using values that are characteristic of those seen in, or calculated from, the observations. (a) The effect of varying n. In this plot, $\mu = 2$ and $\lambda = 8000$ m^{-1}. (b) Changing λ; here $n = 6000$ m^{-3} and $\mu = 2$. (c) μ is varied whilst $n = 6000$ m^{-3} and $\lambda = 8000$ m^{-1}. [Colour figure can be viewed at wileyonlinelibrary.com]

representative of the values seen in the observations. Figure 7a shows that n scales the PSD up or down. Figure 7b shows that λ affects how steep the slope is; the greater the value of λ, the narrower the particle size distribution. In Figure 7c, we show that μ affects the curvature of the PSD. In single moment microphysics schemes, such as the one described in Wilson and Ballard (1999), μ=0, which reduces this function to an exponential distribution.

3.1 | Estimating equivalent gamma PSDs from the observed PSDs

Double moment microphysics schemes predict two quantities: the number concentration of particles and IWC. In our analysis, we compute gamma distributions that have the same moments as our observed PSDs. This is achieved by calculating moments of the observed distributions and using these to calculate the slope parameter, λ, of the gamma distribution. A moment is calculated as

$$m_i = \int_0^\infty N(D)D^i \, dD, \tag{4}$$

where m_i is the moment number, $N(D)$ is the PSD, D is particle diameter, and dD represents the bin width (Rasch & Carslaw, 2022). The number concentration of the gamma distribution is equal to m_0. IWC is dependent on the mass–size relationship of particles, which has the form $m = cD^d$. Previous literature has shown evidence that d is close to 2 (e.g., Brown & Francis, 1995; Heymsfield *et al.*, 2010; Locatelli & Hobbs, 1974). CASIM (Field *et al.*, 2023) uses the mass–size relationship from Cotton *et al.* (2013), where $m = 0.026D^2$, and thus IWC is proportional to m_2. Our analysis is testing what the parameterised PSD would be if m_0 and m_2 were equal to the observations, consistent with the situation where CASIM is correctly predicting the observed number concentration and ice water content.

We use a ratio of the zeroth and second moments to calculate the value of the slope parameter λ in Equation (3). Using Equations (1) and (4), we derive a moment such that

$$m_i = \int_0^\infty n_0 D^\mu \exp(-\lambda D) D^i \, dD. \tag{5}$$

By using the definition of a gamma function, $\Gamma(z+1) = \int_0^\infty t^z \exp(-t)\, dt$, the equation for a moment can be simplified to

$$m_i = \frac{n_0}{\lambda^{\mu+i+1}} \Gamma(\mu + i + 1). \tag{6}$$

Using a ratio of two moments i and j, we derive λ as

$$\lambda = \left(\frac{m_i}{m_j} \frac{\Gamma(\mu + j + 1)}{\Gamma(\mu + i + 1)} \right)^{1/(j-i)}. \tag{7}$$

In this case, $i = 0$ and $j = 2$, relating to n (m_0) and IWC (m_2), as discussed previously. This value for λ is then used in Equation (3), so that the differences presented between the observed and parameterised distributions in Section 4 are not dependent on differing slope parameters.

Based on the particle phase analysis discussed in Section 2.3, particle size analysis, and visual inspection of the particle images, the PSDs analysed in what follows are in the ice phase. Following the hydrometeor classifications used in CASIM, we chose $\mu = 2$ for "snow". Although our analysis is applicable to two moment schemes in general, in what follows we focus on the specific formulation in the CASIM scheme described by Field *et al.* (2023) as an example for two moment schemes.

4 | RESULTS AND DISCUSSION

4.1 | Time series of PSDs and their gamma equivalents

In this section, we examine the PSDs sampled across each of the runs described in Table 2 and compare them with the CASIM distributions. We then explore the quality of the gamma approximation and the microphysical scenarios in which a gamma PSD is a good or bad fit, and what the consequences of that are. The results are presented in the following format:

- First, we show the time series of the PSDs across the run, which provides information about the breadth and shape of the distributions sampled, as well as the variability in those properties across the length of the run (Figure 8).
- Second, we show the equivalent time series of gamma PSDs defined such that m_0 and m_2 are equal to that in the observed data (Figure 9).
- Third, we visualise the ratio between the model and observed PSDs and explore the magnitude and location of significant discrepancies (Figure 10), allowing us to quantify the realism of the gamma distribution at different particle sizes and across different parts of the cloud (Figures 11 and 12).

We examine the PSDs throughout each aircraft run to understand better the variability that occurs between different temperatures, and variability between microphysical regimes at the same temperature. Figure 8 shows the PSD with time through each aircraft run as measured by the HVPS probe. The coloured shading shows the concentration of particles in each size bin. A moving average of 15 s has been applied to improve the representation of less common large particles (Khain *et al.*, 2015) and to help us understand better whether these large particles are associated with a change in microphysical regime. An averaging window of 15 s was chosen as it would take the aircraft approximately 15 s to travel 1.5 km, which is comparable with the grid length of the Met Office UK Variable grid (UKV) model's inner domain. This is also a suitable practical compromise between using a long enough averaging window to improve sample size statistics, without smoothing across differing microphysical regimes. The solid black line on these plots shows the liquid water content (LWC) throughout the run, measured by the CDP. The grey shading shows the segments that will be examined in more detail in later sections (explained in Section 4.2). The time scale bars shown in magenta represent two minutes of each run, and clearly demonstrate that the runs vary in length.

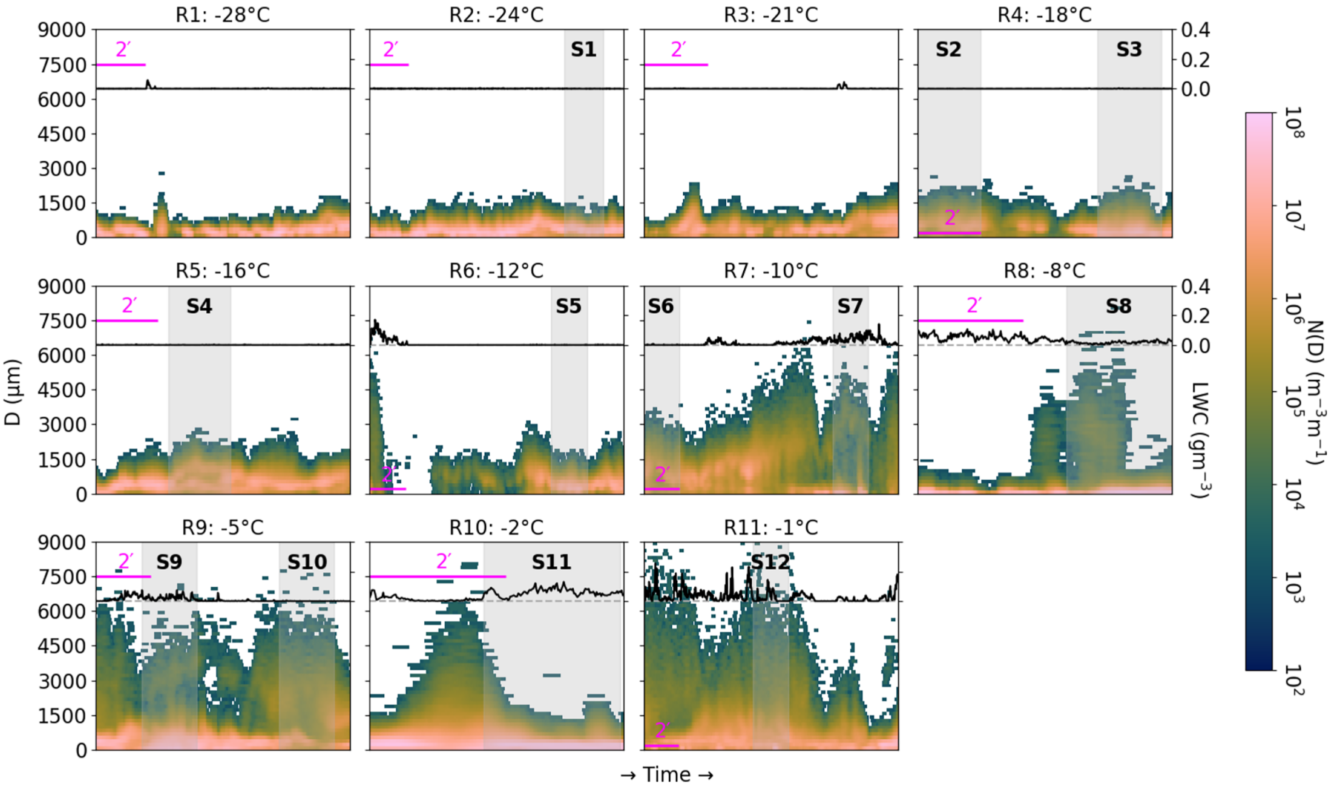

FIGURE 8 15 second moving average of the observed PSD during each run for this case study. The heatmap shows the concentration of particles in each size bin (y-axis) per second (x-axis) using a logarithmic colour scale. LWC measured by the CDP probe (described in Table 1) is shown by the black line, referenced against LWC = 0 gm^{-3}, which is shown by the dashed line. The run number above each panel corresponds to the runs described in Table 2. The shading and labels show the segments that are described in Table 3 and examined in more detail in Section 4.2. Time scale bars representing two minutes of each run are shown on each panel. [Colour figure can be viewed at wileyonlinelibrary.com]

We calculate the PSD per second from the gamma distribution in CASIM using the method described in Section 3. The moments used to calculate the parameterised distribution are the moments from the observations, and we therefore assume that CASIM would perfectly prognose particle concentration and mass mixing ratio to use as the zeroth and second moments. Figure 9 shows the parameterised PSD based on the 15 s moving average of the observed PSD shown in Figure 8. It is important to note that, whereas the observed PSD has a finite width, the parameterised PSD will forecast infinitely small concentrations. This figure shows that, whilst the overall shape of the parameterised PSD with time is similar to the observed PSD, much of the detail and complexity has been smoothed. Since a single gamma distribution cannot represent a multimodal PSD, the PSDs are poorly represented in regions with coexisting particle populations.

To understand in which microphysical regimes the parameterisation performs well, it is useful to compare the observed PSDs (Figure 8) with the CASIM parameterised PSDs (Figure 9). Figure 10 shows the logarithmic ratio between the two distributions. This was calculated by finding the difference between the CASIM parameterised and observed distributions and taking the logarithm of this ratio for each second. In this figure, red represents regions where the PSD from CASIM is greater, and values of 1 occur when the parameterised PSD is 10 times greater than the observed PSD. Blue shows regions where the observed PSD is greater and values of −1 show where the observed PSD is 10 times greater than the parameterised distribution. It is clear that there is no regime where the observed PSD is captured perfectly by the parameterised distribution.

To facilitate the discussion, we have grouped the runs with comparable microphysical characteristics. These are presented in the following subsections.

4.1.1 | Runs containing polycrystals

At cold temperatures and low saturation near the cloud top, the microphysical regime favours the growth of small polycrystals (Takahashi *et al.*, 1991), and indeed we see from Table 2 that the dominant crystal habits in R1–R5

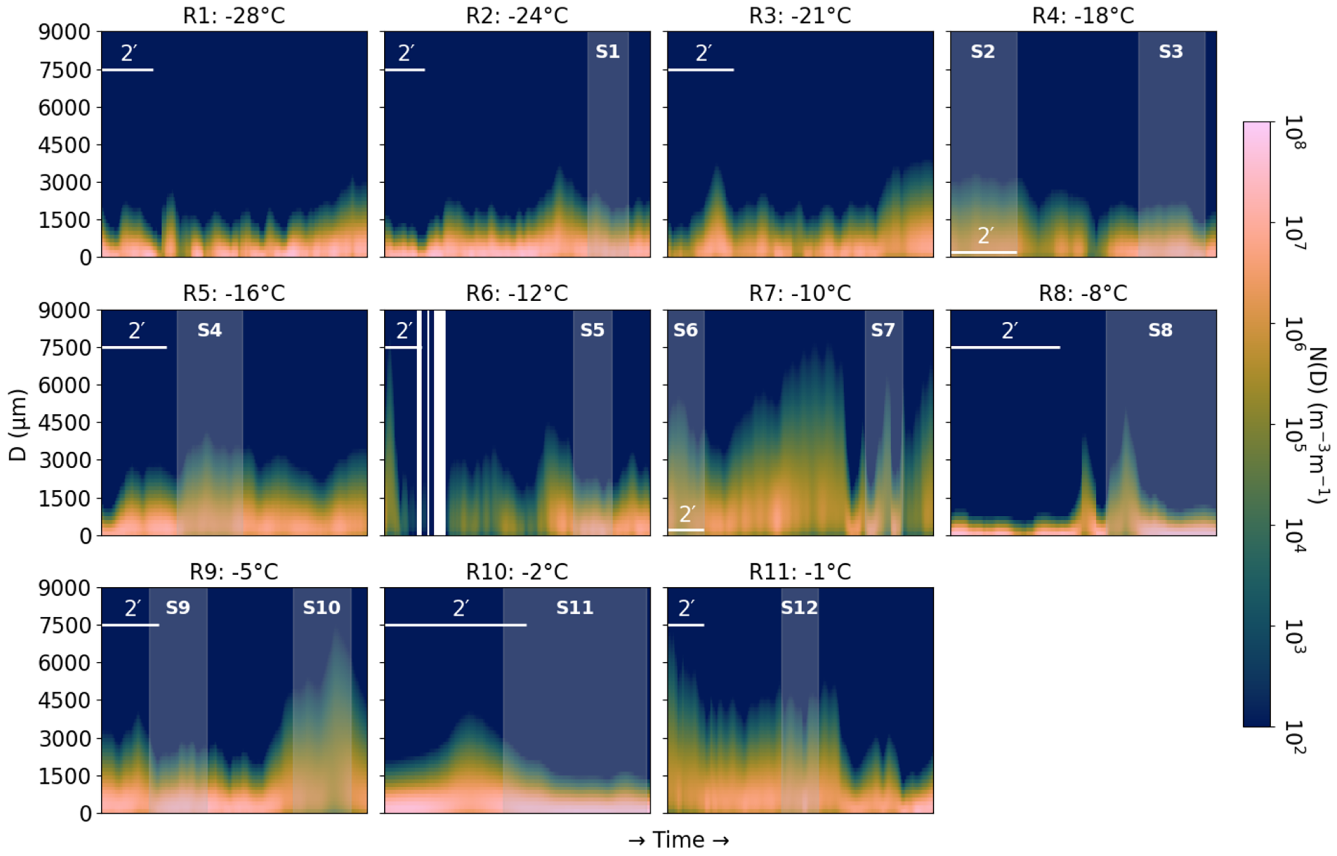

FIGURE 9 As Figure 8, but for the CASIM parameterised PSD during each run for this case study. Time scale bars representing two minutes of each run are shown on each panel. [Colour figure can be viewed at wileyonlinelibrary.com]

are polycrystals. From Figure 8, we see that R1–R5 have similar PSD shapes; however, the width of the PSD and size of particles with peak concentrations increases with temperature. A common feature among all of these runs is the absence of liquid water. In R1 and R2, particles are less than 1.5 mm in size, with peak concentrations at sizes of 300–500 μm. There is minimal change in this structure throughout these runs, which is indicative of a single mode of particles existing in these regimes. R3 has some variation in PSD width, ranging from approximately 1–2 mm, and peak particle concentration size, ranging from 0.5–1 mm. However, the monomodal structure of the PSD suggests a single particle population exists in this run. There is more variation in the PSD shape in R4. The maximum particle size remains relatively consistent throughout at approximately 1.5–2.5 mm; however, we can see differences in the magnitude and size of the peak concentrations clearly. In the first half of the run, we see that the peak concentration is at around 750 μm, whereas in the later half of the run the peak concentration is smaller at less than 500 μm. In R5, we see that the PSD has become broader, with maximum particle sizes up to almost 3 mm. The peak particle concentration remains fairly constant at around 500 μm, apart from a region near the middle where the distribution becomes bimodal, with two weaker concentration peaks surrounding 500 μm. This is indicative of a larger and a smaller mode of particles coexisting here. Comparing this with Figure 9, we see that, generally, the structure and width of the PSD in these runs appears to be captured relatively well. There is a less well defined peak concentration size in the parameterised PSDs, and the clear bimodal feature in R5 that is visible in Figure 8 is not represented in the parameterised distribution. This is because a single gamma distribution cannot physically represent a bimodal distribution. Figure 10 shows the differences between the observed and parameterised distributions more clearly. We see that in R1–R3 the observed PSD is narrower than the parameterised PSD. This is evident from the high values at the smallest and largest ends of the distribution. It is also clear that the parameterisation does not capture the magnitude of the peak concentration accurately. This suggests that using a higher value of μ would capture the shape of the observed PSDs in these runs better, as the value of μ affects the shape of the distribution (demonstrated in Figure 7c). This same pattern is apparent in most of R4, with the exception of a period near the end of the run, where the observed distribution is broader than the parameterised distribution. This corresponds to

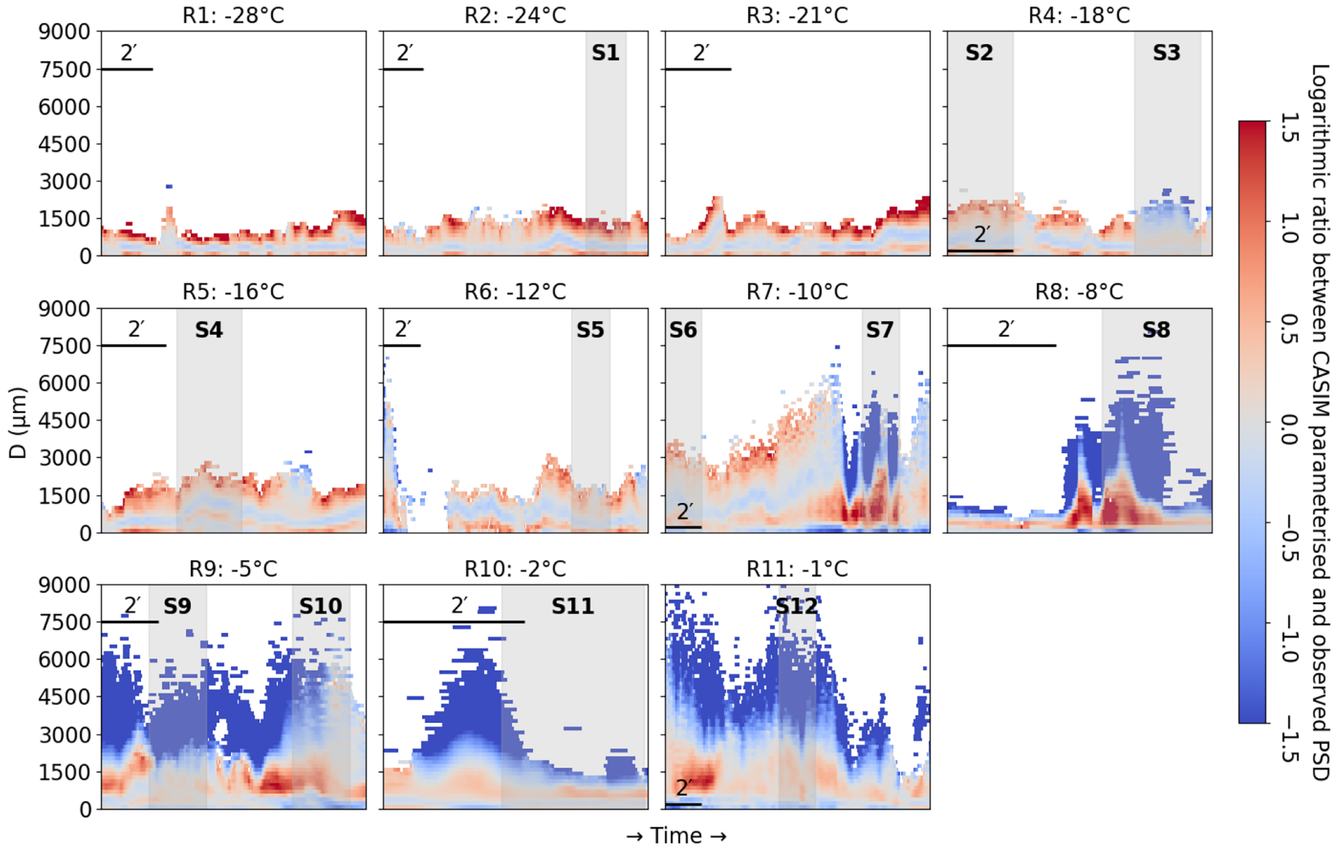

FIGURE 10 Logarithmic ratio between the observed and CASIM parameterised concentrations. Positive values show where the parameterised distribution is greater than the observed distribution and negative values show where the observed distribution is greater than the parameterised distribution. Shading and panel labels as in Figure 8. Time scale bars representing two minutes of each run are shown in black. [Colour figure can be viewed at wileyonlinelibrary.com]

the region with high concentrations of very small particles that is clear in Figure 8. Very small particles have low mass but high concentrations; as CASIM is dependent on the zeroth moment, it is weighted towards those particle sizes with the highest concentration and therefore does not capture the width of the observed PSD accurately here. We see more variation in the differences between the observed and parameterised PSDs in R5. The area with the observed bimodal PSD is very clear in this plot, and there is also a brief period where the observed PSD is broader than the parameterised PSD. This is likely due to a slightly increased concentration of very small particles.

4.1.2 | Runs containing dendrites

As the temperature increases, the PSD changes shape due to the dendritic particle habits that form at these temperatures, as shown in Table 2. The temperatures of these runs are warmer than the temperatures typically associated with the dendritic growth regime (Libbrecht, 2005; Takahashi *et al.*, 1991), so we suggest that the dendrites observed in these runs have sedimented from higher altitudes. We start to see more variation between runs, but also between different regions at the same temperature. We also start to see the presence of liquid water, which adds to the complexity of the microphysics. It is important to note that liquid particles will not influence the PSD, as they are too small to be observed by the HVPS probe (discussed in more detail in Section 2.3 and demonstrated in Figure 5). From Figure 8, we see that there is a range of PSD widths and structures in R6. At the beginning of the run, there is a relatively low concentration of large particles, with maximum sizes of up to 6 mm. This population does not persist, and is instead replaced by a population of much smaller particles with a maximum size of approximately 1.5 mm, but which are also present in low concentrations. It is clear that there is then a shift in microphysical regime, as the maximum particle size increases to around 2–2.5 mm and the concentration of particles increases, with the peak concentration size at approximately 500 μm. In R7, the particle size increases significantly, ranging from 4 to 6 mm across the run, resulting in a much broader PSD than those seen at colder temperatures. There is also a distinct regime change in this run, which seems to correspond to the presence of increased liquid water. In the first half of the run, the highest concentration of particles is around 1.5 mm. In the latter half of the run, there are very high concentrations of very small particles, which exist alongside another low concentration population of much larger crystals. The microphysical regime in R8 appears to be quite different, with a persistent population of numerous small particles, with maximum particle sizes of this population remaining under 1.5 mm. However, there exists another short lived population of much larger particles with maximum sizes exceeding 6 mm. We would expect these two populations to have distinctly different microphysical properties.

From Figure 9, we see that the shape of R6 is captured well by the parameterised PSD, with changes in the magnitude of the peak concentration parameterised correctly. Figure 10 confirms this, as we see that the parameterised PSD overestimates the smallest and largest particles slightly and underestimates the peak concentration, but generally is a good fit. The short lived larger mode of particles at the beginning of R6 is less well represented by the parameterisation, with the smallest and largest particles being underestimated and the peak concentration overestimated, in contrast to the rest of the run. Figure 9 shows that the early half of R7 is captured relatively well by the parameterisation, but the regime with very high concentrations of small particles is not represented well by the parameterised PSD. Likewise, the parameterised PSD does not capture the full width of the observed PSD in R8. This is because, as explained in Section 4.1.1, CASIM is weighted towards the particle size with the highest concentration. This is clear from Figure 10, where we see that the very small mode of particles in both R7 and R8 is underestimated significantly by the parameterised PSD. The peak concentration of these modes is overestimated, and the parameterisation does not capture the tail of the observed distribution, meaning the large particles are not represented at all.

4.1.3 | Runs containing needles

We expect the microphysical properties of the cloud to change again with increased temperature, with needle and column growth types being dominant at temperatures of −8 to −3° C (Bailey & Hallett, 2009; Hueholt *et al.*, 2022). In Table 2, we see that the dominant particle habit in R9–R11 is needle-like or columnar. There is evidence to suggest that SIP is influencing the PSDs in these microphysical regimes due to the very high concentration of small particles observed. There are three SIP mechanisms to be considered: the Hallett–Mossop (or rime splintering) mechanism (Hallett & Mossop, 1974), ice–ice collisional fragmentation, and freezing droplet fragmentation. The correlation of high concentrations of small particles with the presence of liquid water suggests that ice–ice collision is not the dominant ice multiplication mechanism in this case, and that it is not acting independently of a different SIP mechanism. Droplet fragmentation has been studied primarily in the laboratory (e.g., Lauber *et al.*, 2018; Phillips *et al.*, 2018) or in convective clouds (e.g., Lauber *et al.*, 2021) and is therefore not well understood in frontal clouds. However, we see from Table 2 that drizzle is observed infrequently, and later in Table 3 that secondary particles are observed when drizzle is not present. We argue that this and further evidence presented in Section 4.2 justifies focusing on the Hallett–Mossop mechanism in the analysis that follows. It is also likely that other particle types that have precipitated from higher layers of the cloud are influencing the PSDs in these runs. Figure 8 shows that the range of particle sizes in R9 is broad, with particles of more than 6 mm being observed throughout the run. In the early half of the run, concentrations of these large particles are low, whereas the concentration of particles less than 1 mm in size is very high. This, combined with the presence of liquid water, is indicative of rime splintering occurring. In the latter part of the run, the concentration of this population of very small particles drops significantly and the concentration of larger particles increases. In R10 there is a persistent, high concentration population of very small particles with a peak concentration size of less than 750 μm and maximum size of up to 1.5 mm. This population coexists with liquid water, which suggests that SIP may be contributing to the high concentration of particles observed here. When the liquid water content is low in this run, the PSD width increases notably, with particles over 6 mm observed, whilst the concentration of the small particles decreases slightly. In R11, the PSD width is very broad, with maximum particle sizes up to 9 mm in parts of the run. The population of very small particles that is present in R9 and R10 does not appear to be present in R11, and instead the concentrations appear generally to be distributed more evenly among particle sizes. The PSD width decreases towards the end of the run, and the population of very small particles is observed for a short period at the end of the run. It is clear from Figure 9 that the parameterised PSD performs poorly in the runs presented in this section. Whilst the shape of the observed PSD is captured broadly by the parameterisation, the width of the parameterised PSD is significantly narrower than the observed one. Figure 10 verifies this, as we see that the parameterised PSD overestimates the peak concentration of particles substantially and underestimates the concentration of small and large particles. In

TABLE 3 A summary of the segments studied in closer detail in this section. Note that the segment numbers are based on altitude/temperature, not time. The particle habits in **bold** show the most common particle shape, with descending frequency listed sequentially. LWC has units of $\mathrm{kg\,m^{-3}}$.

Segment number	Temperature (°C)	Particle habits	Key features
S1	−24	**Polycrystals**, plates	Narrow PSD width, ice only
S2	−18	**Polycrystals**	Narrow PSD width, ice only
S3	−18	**Polycrystals**	Narrow PSD width, ice only
S4	−16	**Polycrystals**, plates, columns	Bimodal PSD, ice only
S5	−12	**Polycrystals**, columns, plates	Narrow PSD width, ice only
S6	−10	**Dendrites**, polycrystals	Broader PSD width, ice only
S7	−10	**Dendrites**, drizzle, aggregates	Bimodal PSD, cloud droplets present
S8	−8	**Dendrites**, drizzle, aggregates	Bimodal PSD, cloud droplets present
S9	−5	**Needles**, columns, drizzle, dendrites, aggregates	Secondary ice particles present, cloud droplets present
S10	−5	**Dendrites**, columns, aggregates	Bimodal PSD, ice only
S11	−2	**Needles**, columns, plates, ice lollies[a]	Secondary ice particles present, cloud droplets present
S12	−1	**Needles**, columns, dendrites, aggregates	Bimodal PSD, cloud droplets present

[a] As described in Keppas *et al.* (2017).

R9 and R10, this is due to the population of high concentration, small particles seen in Figure 8, which weights the parameterised distributions towards small particles. This means that the large particles coexisting with this population are not represented by the parameterisation. In R11, large particles are also not represented by the parameterised PSD. This suggests that, although the concentration of very small particles is lower in this run compared with R9 and R10, is it significant enough to weight the parameterisation towards small particles, which therefore means it fails to capture the width of the observed PSD.

4.2 | Exploring the microphysical structure in more depth

In this subsection, we analyse smaller segments of the aircraft time series to understand the microphysical properties of the cloud in greater depth for the different regimes discussed in Sections 4.1.1–4.1.3. This includes segments with a range of LWCs, PSD widths, microphysical processes such as SIP and particle habits. Table 3 lists 12 segments, each two minutes long, extracted from the full time series in Figure 8. The time interval of each segment is indicated by the grey shading and labelled in Figures 8–10. These segments were selected to be reasonably homogenous.

To understand better the fundamental microphysical changes between different regimes, we calculate an average observed PSD per segment, which is shown in Figure 11. Also shown in Figure 11 are the gamma-equivalent PSDs for comparison. This figure clearly shows the changes in observed PSD shape in different microphysical regimes, and demonstrates how the parameterisation has a varied performance between these regimes.

We examine ice crystal shape data for the same segments. We calculate the area ratio for each image sampled in the segment, defined as the ratio of particle area to that of a circle with a diameter equal to the maximum particle dimension, and bin the data by particle diameter. We use area ratio as a metric of particle shape. When distinct ice crystal types are present in the same cloud volume, such as needles and polycrystals, they often appear as distinct modes in these area ratio distributions. We use this to inform our interpretation of the PSDs. Figure 12 shows a normalised 2D histogram of particle concentrations for each area ratio and size bin, and the grey line shows the median area ratio for each size bin. A higher area ratio means the particle is more circular.

4.2.1 | Segments containing polycrystals

The segments in the colder parts of the cloud system display a broadly similar pattern, and one that is consistent with the analysis in Section 4.1.1. From Figure 11, we see that the PSD is monomodal and quite comparable in shape to a gamma distribution. However, even here there are non-negligible differences in the detailed distributions. In S1 and S2, we observe that the gamma fit

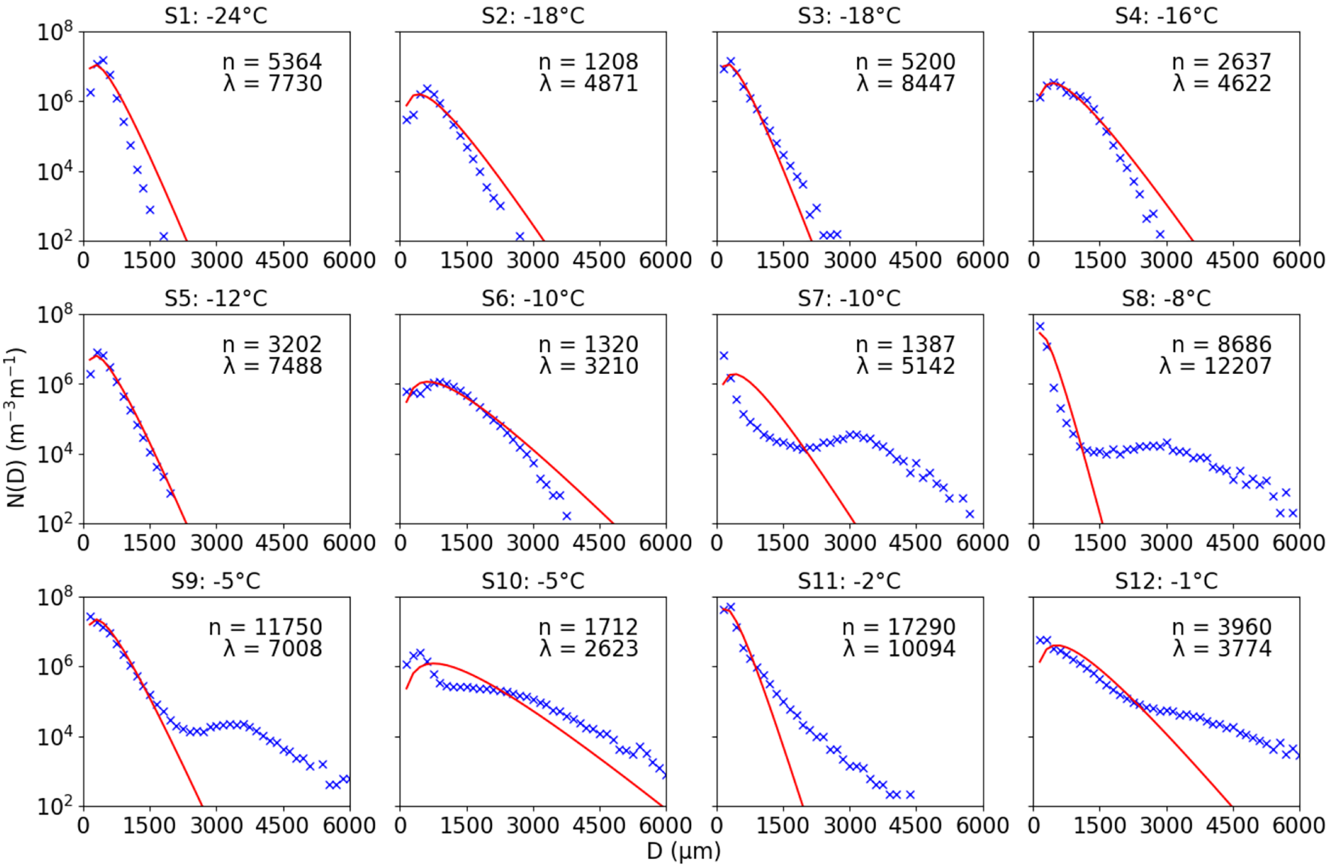

FIGURE 11 Average PSDs from each 2 minute segment, labelled above each panel and described in Table 3. Observations are shown by the crosses and the CASIM parameterised PSD is shown by the solid line. The mean values of particle concentration (n, in m^{-3}) and λ (in m^{-1}) for each run are shown in each subplot. [Colour figure can be viewed at wileyonlinelibrary.com]

overestimates the concentration of particles greater than 1 mm, while underestimating the peak of the distribution. In S3 we see the opposite; the peak is well captured, but the tail of particles larger than 1 mm is underpredicted. S4 has a slightly bimodal structure, with a mode near 500 μm and another near 1250 μm, which suggests that multiple snowflake populations may be developing even at this level. The first peak is captured well, but the second peak is not represented in the parameterised distribution and the tail of particles greater than 1 mm is overestimated. Figure 12 shows that the area ratios of these cold particles decrease systematically with particle size, in a manner similar to that reported elsewhere (e.g., Heymsfield *et al.*, 2013). The pattern of this decrease is similar across S1, S2, and S3 due to the homogeneity of particles in these segments. An example of the particles seen in S1 is shown in Figure 13, where it is clear that polycrystals of relatively consistent sizes are the dominant crystal type in this regime. However, in S4 we observe a slight inflection of the median area ratio as a function of diameter at around 1250 μm, which corresponds with the second peak in the PSD seen in Figure 11, and note that the area ratio of particles greater than 1 mm is systematically higher than in S1–S3. Figure 14 shows the particles observed in this segment, which provide evidence to suggest that there are two coexisting particle populations: a population of polycrystals, which have possibly precipitated from higher altitude cloud layers, and a population of plate-like crystals, which are characteristic of particles that have formed at this temperature (Takahashi *et al.*, 1991).

4.2.2 | Segments containing dendrites

Figure 11 shows that the PSDs in S6, S7, and S8 are poorly represented by the gamma parameterisation. The observed PSD in S6 is broad; however, the concentration of larger particles and maximum observed particle size is overestimated by the parameterised distribution. The observed PSDs in S7 and S8 show a similar bimodal pattern, with very high concentrations of small particles but broad ranges of particle sizes, as discussed in Section 4.1.2. The concentrations of small and large particle modes are shown in Table 4 and show that the concentration of the small particle mode in S7 and S8 comprises the majority of the particle concentration across the whole size

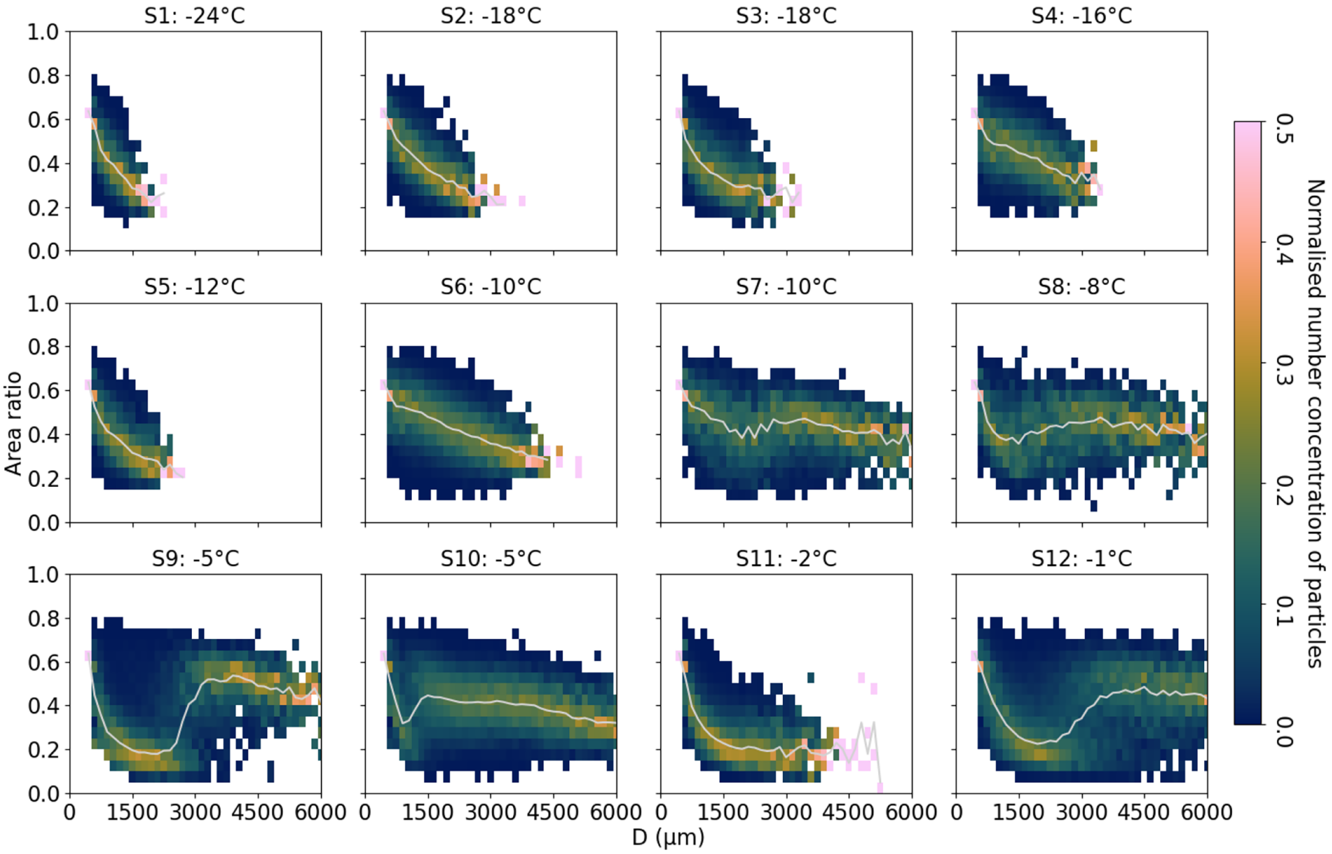

FIGURE 12 Area ratios by segment, labelled above each panel and described in Table 3. Each particle observed in each run was binned according to particle size and calculated area ratio. Each bin has been normalised by the total number of particles in each size bin. The solid line shows the median area ratio for each size bin. [Colour figure can be viewed at wileyonlinelibrary.com]

distribution. This leads to extremely poor representations of the observed PSD by the parameterised distribution. The concentrations of the smallest particles are underestimated due to the shape of the gamma distribution, but the concentrations of the rest of the population of small particles are overestimated. The population of larger particles is not represented at all by the parameterisation. Figure 12 provides evidence to suggest that these segments are being influenced by populations of small particles that weight the parameterised distribution towards these small particles. Particles in S6 have a largely uniform distribution of area ratios; however, there is a small inflection in the median area ratio in the first two size bins that indicates a slightly different particle population that is influencing the PSD. There are clearly two distinct particle populations in both S7 and S8, with a small population of particles the area ratios of which broadly follow the profiles seen in the colder runs. At sizes $\gtrsim$ 1–2 mm, the dominant population becomes the larger particles, which have a remarkably consistent area ratio across the broad range of sizes observed. The total observed particle concentrations displayed in Table 4 are an order of magnitude higher than predicted ice nuclei concentrations based on temperature from DeMott *et al.* (2010) in each segment discussed in this section. Whilst ice nuclei concentrations are also dependent on numerous other factors such as season and location, this relationship provides an approximate value to compare with the observed ice concentrations. The concentration of large particle modes is comparable with the estimated ice nuclei concentrations, which is consistent with the dendritic particle populations in these segments forming by primary nucleation. As mentioned in Section 4.1.2, the temperatures of these segments are warmer than we would expect for the formation of dendrites, which therefore suggests that these particles have formed at slightly higher altitude, where active ice nuclei are slightly more numerous. The high concentrations of the small mode of particles are comparable with the concentration of ice particles observed in colder runs, shown in Table 2, which could be evidence that the small mode of particles consists of polycrystals that sediment from higher altitudes. Figure 15 may support this suggestion, as a population of large dendritic crystals is visible in the HVPS images, but there is also evidence from the 2DS images that a population of small polycrystals (~ few hundred microns in diameter) is present.

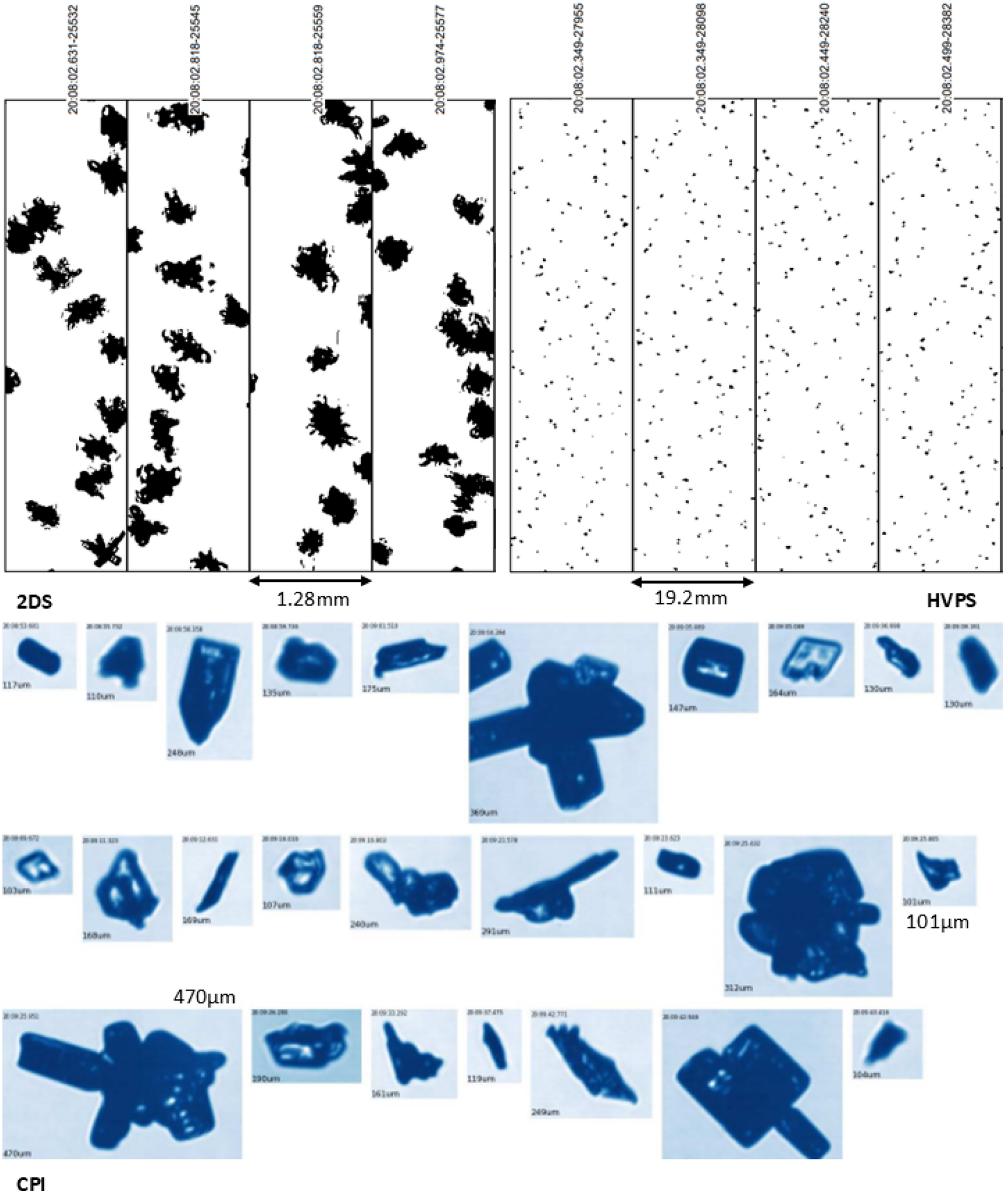

FIGURE 13 Example images of the homogenous polycrystals from S1, as described in Table 3. The array width of the 2DS probe is 1.28 mm and that from the HVPS probe is 19.2 mm. The smallest and largest particles from these CPI images have the sizes written adjacently for scale. [Colour figure can be viewed at wileyonlinelibrary.com]

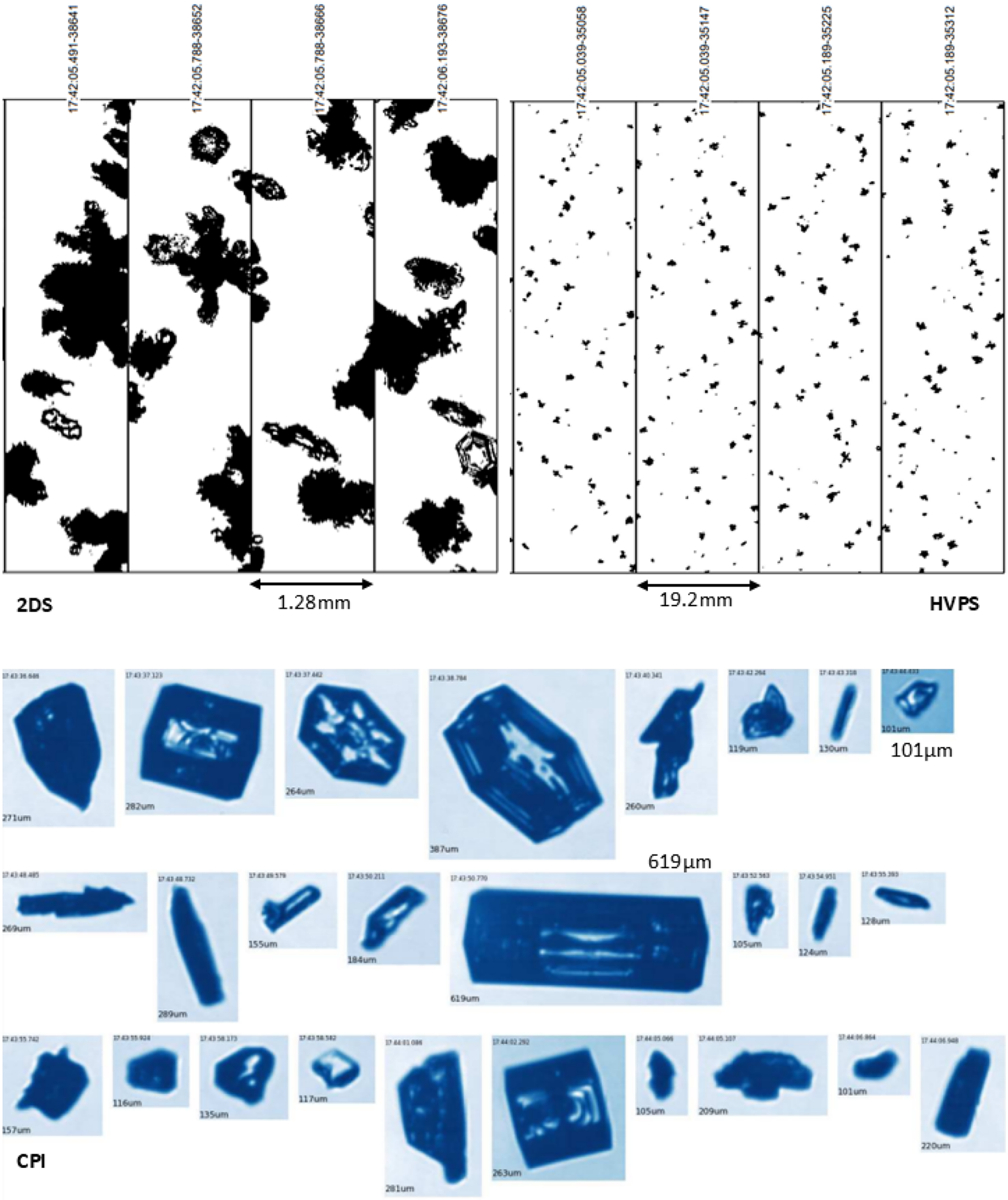

FIGURE 14 As Figure 13, but for S4. The HVPS images clearly show that there are larger and smaller particles. The 2DS images show that there are coexisting populations of plate crystals and polycrystals in this segment. [Colour figure can be viewed at wileyonlinelibrary.com]

TABLE 4 A summary of the concentrations of different particle modes discussed in Section 4.2.2. The segment numbers correspond to those described in Table 3. INC refers to ice nuclei concentration. 75 μm is the minimum particle size observable by the HVPS probe.

Segment	Total concentration (m^{-3})	Small mode size range (μm)	Small mode concentration (m^{-3})	Large mode size range (μm)	Large mode concentration (m^{-3})	Predicted INC[a] (m^{-3})
S6	1320	75–500	382	> 500	938	408
S7	1387	75–2000	1337	> 2000	50	408
S8	8686	75–1500	8651	> 1500	35	318

[a] Estimated by $0.117\mathrm{e}^{-0.125T_\mathrm{C}}$, where T_C is the temperature in °C. As described in DeMott *et al.* (2010).

4.2.3 | Segments containing needles

The distribution of particle sizes at higher temperatures is also poorly represented by the parameterised distributions. Figure 11 shows that these segments are heavily influenced by populations of very small particles that coexist with populations of larger particles, which is clear from the bimodal nature of the observed PSDs. In S9, we see that the observed PSD profile is very similar to that seen in S7 and S8, with high concentrations of very small particles, but with a coexisting population of large particles with a broad size range. Despite being at the same temperature, the observed PSD profile of S10 is noticeably different from that of S9. The broad size range remains, but the concentrations of the smallest particles are much lower and the particle size with the greatest concentration is around 500 μm. In S11 we see that the concentration of small particles is again very high, but the range of particle sizes is narrower. In contrast, the profile of S12 is similar to that of S10; however, the concentration of the smallest particles is higher. All of these segments are poorly represented by the parameterised PSD, with the concentration of small particles being slightly underestimated and the population of large particles often being completely missed. Similarly to the segments discussed in Section 4.2.2, Figure 12 shows that populations of small particles are influencing the PSDs in these segments. However, these populations have different characteristics from the populations of small particles examined in Section 4.2.2. In S9, there are very clearly two populations of particles with different characteristics. The smaller particles with sizes less than 2.5 mm have very low area ratios, generally below 0.3, which is evidence that this population is formed of needle and column crystals. Particles greater than 2.5 mm have a much higher area ratio of 0.4 or greater. This distinct population of small, needle-like crystals and the presence of liquid water as shown in Figure 8 provide evidence that SIP is influencing the PSD in this segment. The Hallett–Mossop rime splintering process (Hallett & Mossop, 1974) produces small ice splinters, which are too small to be observed directly by the OAPs, but these splinters grow into needle and column crystals that have very low area ratios, like those seen in Figure 12. Figure 16 provides evidence to support this, as it shows that high concentrations of needle crystals were observed in this segment, together with larger dendritic crystals, which form the population of particles with higher area ratios. The particle concentrations shown in Table 5 also provide evidence for this. The concentration of the small particle mode in this segment is two orders of magnitude higher than the predicted ice nuclei concentration estimated by temperature alone (DeMott *et al.*, 2010), which is consistent with findings from previous studies (Mossop *et al.*, 1972). We see this population of small, non-spherical particles persist in S11 and S12. As the Hallett–Mossop process does not typically occur at these temperatures, we infer that the small particles produced in S9 have precipitated into lower layers of the cloud. The particle concentrations displayed in Table 5 support this theory, as we see very high concentrations of the small particle mode relative to the concentration of larger particles, if indeed they exist, and the concentrations of small particles are one to two orders of magnitude higher than the predicted concentration of ice nuclei. Figure 17 shows the particles observed in S11, and there is evidence of mature secondary ice crystals including ice lollies (Keppas *et al.*, 2017) and heavily rimed particles. Ice lollies form when a column crystal collides with a drizzle drop, and may increase ice crystal concentrations through secondary particle generation. However, whereas this small particle mode is the only particle population in S11, in S12 we observe a coexisting population of large, rounded particles with high area ratios, which suggests this second mode is aggregates. In S10, the population of small particles is almost non-existent, which is consistent with the PSD shown in Figure 11. Figure 8 shows that this segment has no liquid water present, which explains the absence of needle-like crystals, as the Hallett–Mossop process requires the presence of liquid water to produce ice splinters. Table 5 also shows that the concentration of small particles in this segment is significantly lower than in the other segments shown, though interestingly the concentration is still an order of magnitude higher than the predicted ice nuclei concentration,

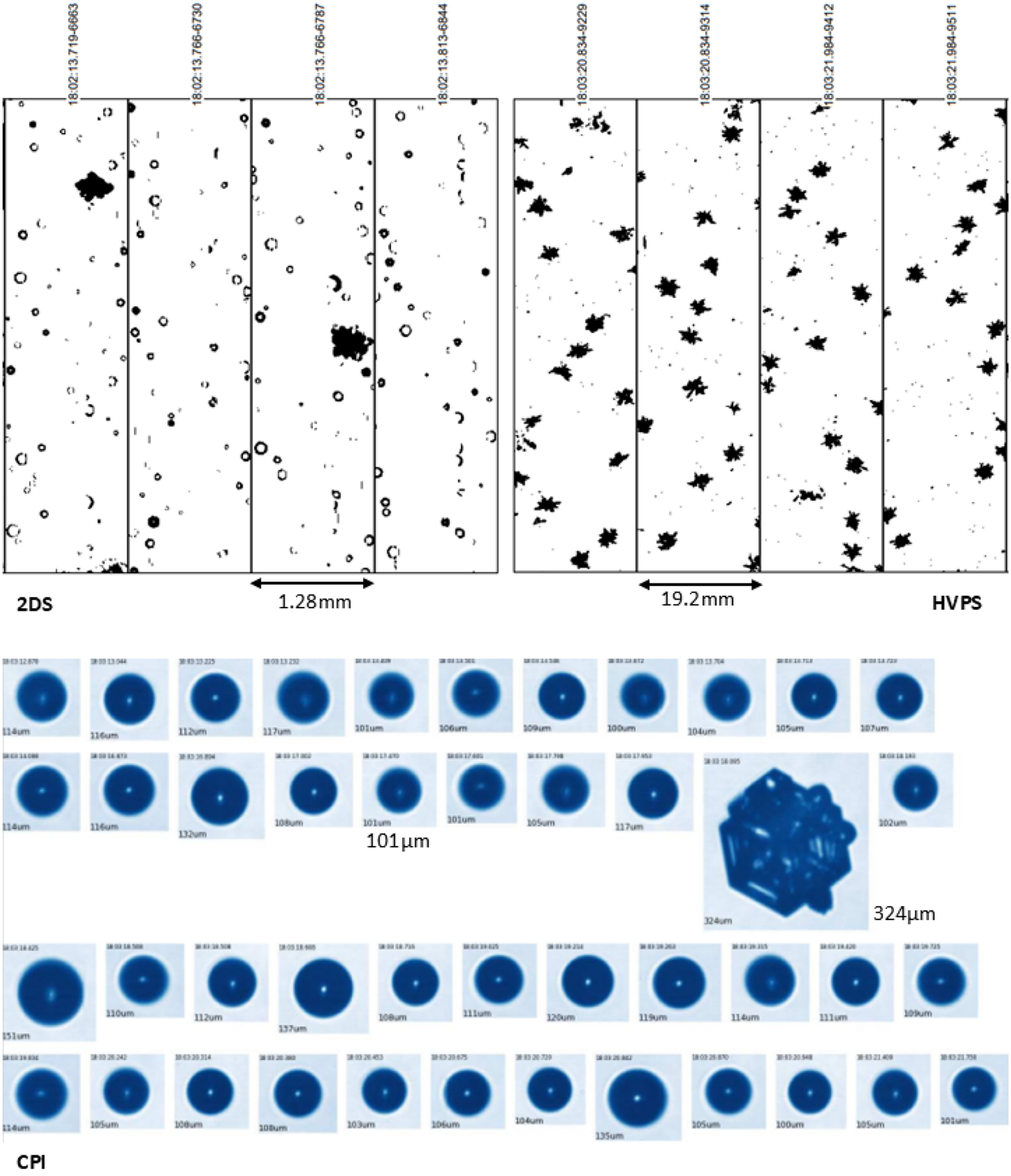

FIGURE 15 As Figure 13, but for S7. The HVPS probe shows that the population of larger particles here are dendrites and the 2DS and CPI images show the presence of drizzle drops. [Colour figure can be viewed at wileyonlinelibrary.com]

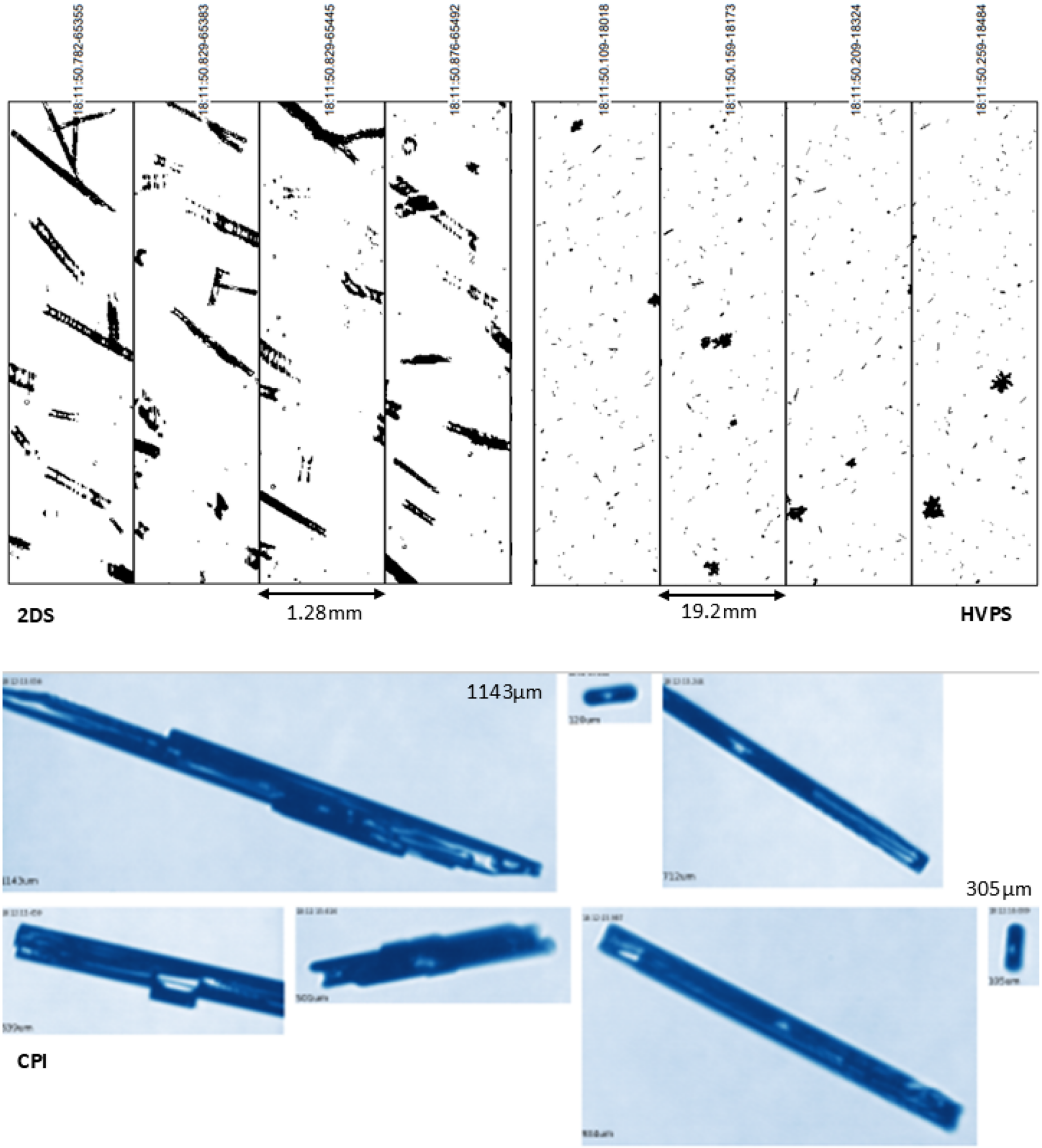

FIGURE 16 As Figure 13, but for S9. We see here needle crystals imaged by the 2DS probe. The HVPS images show that these appear in high concentrations, but that there are also dendrites present which contribute to the broad width of the PSD observed here. [Colour figure can be viewed at wileyonlinelibrary.com]

TABLE 5 A summary of the concentrations of different particle modes discussed in Section 4.2.3. The segment numbers correspond to those described in Table 3. INC refers to ice nuclei concentration. 75 μm is the minimum particle size observable by the HVPS probe.

Segment	Total concentration ($\mathrm{m^{-3}}$)	Small mode size range (μm)	Small mode concentration ($\mathrm{m^{-3}}$)	Large mode size range (μm)	Large mode concentration ($\mathrm{m^{-3}}$)	Predicted INC[a] ($\mathrm{m^{-3}}$)
S9	11750	75–2500	11718	> 2500	32	219
S10	1712	75–1000	1242	> 1000	470	219
S11	17290	> 75	17290	—	—	150
S12	3960	75–2500	3874	> 2500	86	133

[a] Estimated by $0.117\mathrm{e}^{-0.125T_\mathrm{C}}$, where T_C is the temperature in °C. As described in DeMott *et al.* (2010).

which suggests secondary ice particles are present in this segment, despite not being actively produced.

4.3 | Comparison of process rates and moments from observed PSDs versus gamma fits

The importance of representing PSDs accurately in numerical weather models becomes apparent when model process rates and forecast products are calculated, and it becomes clear that inaccurate PSDs cause misrepresentation of these variables. In sections 4.1 and 4.2, we have observed that there are significant differences between the observed PSDs and their gamma equivalents. In this Section, we detail the calculations made for process rates (vapour growth and aggregation) and moments (precipitation rate and radar reflectivity) using both the observed and parameterised PSD time series (detailed in Table 2) to gauge the significance of those differences for the evolution of the model microphysics and for its prediction of the cloud characteristics.

We calculate the percentage change between precipitation, vapour growth and aggregation rates, and radar reflectivity calculated from both the observed and parameterised PSDs. All constants are displayed in Table 6. We estimate particle mass using the mass–size relationship of the familiar form $m = cD^d$, where D is the particle diameter in metres and we use the values for the constants c and d described in Cotton *et al.* (2013). The terminal velocity of particles is estimated by

$$v = aD^b\left(\frac{\rho}{\rho_0}\right)^f,$$

where ρ is the density of air (we use $1\,\mathrm{kg\,m^{-3}}$ in our calculations for simplicity), ρ_0 is the reference density of air, and a, b, and f are constants defined in Field *et al.* (2023). Using these estimations, we calculate precipitation rate in $\mathrm{m\,s^{-1}}$ by

$$r = \frac{\int N(D)mv\ dD}{\rho_\mathrm{water}}, \tag{8}$$

where ρ_water is the density of liquid water and dD is the resolution of the OAP.

The vapour growth rate of ice crystals is calculated by

$$\psi = \xi \int CFN(D)\ dD, \tag{9}$$

where $C = D/2$ is the capacitance of a sphere. ξ is defined as $\xi = 4\pi D_\mathrm{v}(\Delta\rho)$, where D_v is the diffusivity of water in air and $\Delta\rho$ is the difference in vapour density between the surface of an ice crystal and its environment. As we take the ratio between the vapour growth rates calculated from the observed and parameterised PSDs, D_v and $\Delta\rho$ are never calculated explicitly. F is defined as the ventilation factor, which represents the increased transport of vapour when the particle is falling compared with when it is stationary, and is given by $F = 0.78 + 0.31\mathrm{Sc}^{1/3}\mathrm{Re}^{1/2}$, where Sc is the Schmidt number and Re is the Reynolds number, defined by $\mathrm{Re} = vD/v_k$, where kinematic viscosity $v_k = \eta/\rho$ and η represents dynamic viscosity.

We calculate the aggregation rate by

$$W = \iint K_{xy}N(D_x)N(D_y)\ dD_x\ dD_y, \tag{10}$$

where x and y represent the two PSDs involved in the aggregation process (Pruppacher & Klett, 1997) and

$$K_{xy} = \frac{\pi}{4}E_\mathrm{agg}(D_x + D_y)^2|v_x - v_y|.$$

Field *et al.* (2023) assume the aggregation efficiency of particles $E_\mathrm{agg} = 0.1\mathrm{e}^{0.08T_\mathrm{c}}$, where T_c is the temperature in degrees Celsius.

Radar reflectivity is calculated by

$$Z = \frac{36\times10^{18}}{\pi^2\rho_\mathrm{ice}^2}\frac{|k_\mathrm{ice}|^2}{|k_\mathrm{water}|^2}\int m^2N(D)\ dD \tag{11}$$

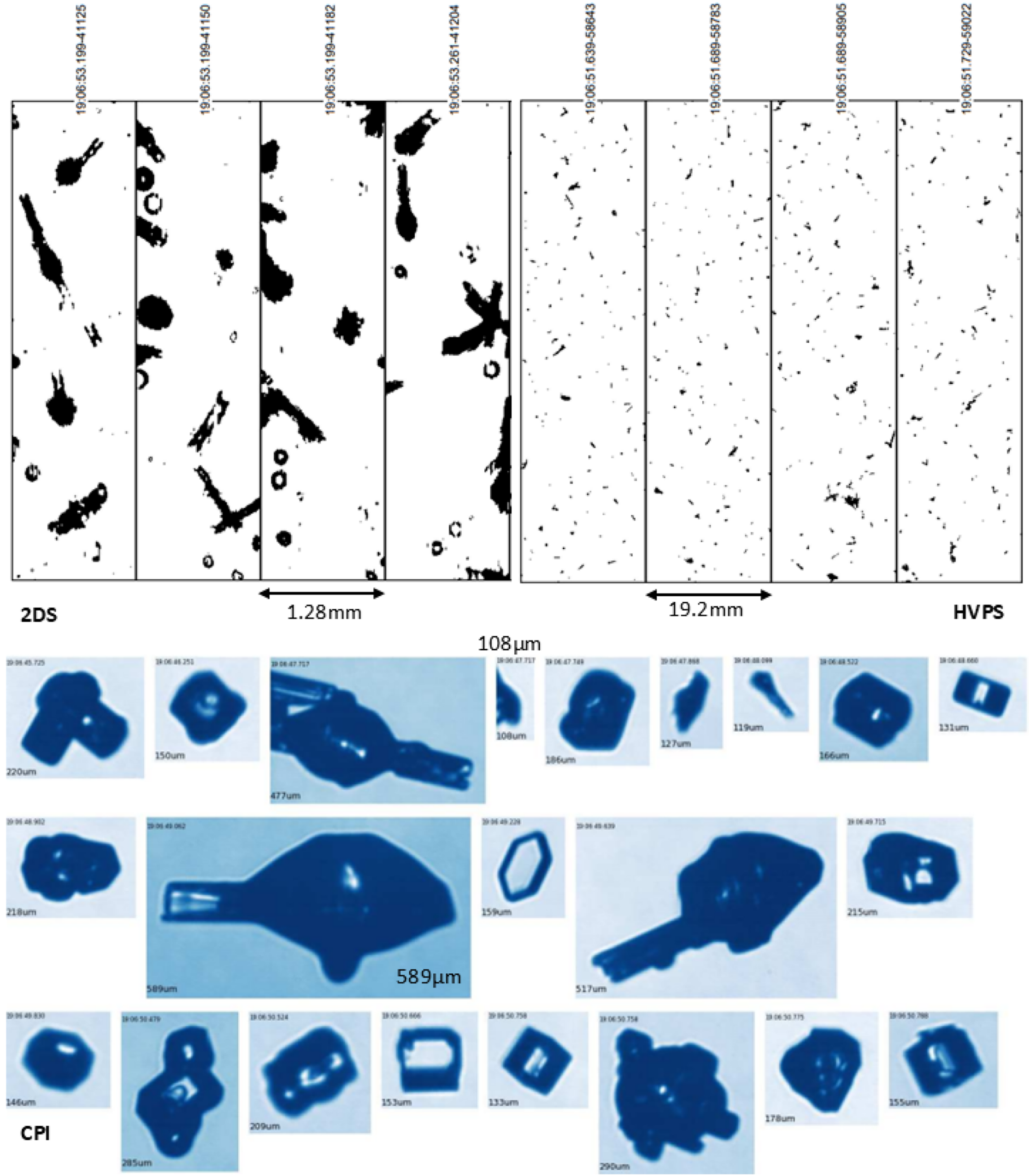

FIGURE 17 As Figure 13, but for S11. We see needle and ice lolly crystals imaged by the 2DS. The CPI images from this segment show that a mix of particle habits are present and that there is evidence of riming. [Colour figure can be viewed at wileyonlinelibrary.com]

TABLE 6 Definitions for all constants used in process rate calculations in Section 4.3.

Term	Constant
c	0.026[a]
d	2[a]
a	12[b]
b	0.5[b]
f	0.5[b]
ρ_0	$1.22\,\mathrm{kg\,m^{-3}}$
ρ_{water}	$1000\,\mathrm{kg\,m^{-3}}$
Sc	0.63[c]
η	$1.7\times10^{-5}\,\mathrm{N\,s\,m^{-2}}$
$\lvert k_{\mathrm{ice}}\rvert^2$	0.174
$\lvert k_{\mathrm{water}}\rvert^2$	0.93
ρ_{ice}	$917\,\mathrm{kg\,m^{-3}}$

[a] Cotton *et al.* (2013).
[b] Field *et al.* (2023).
[c] Field *et al.* (2008).

(Wood *et al.*, 2013, 2014), where $|k_{\mathrm{ice}}|^2$ and $|k_{\mathrm{water}}|^2$ are the dielectric factors for ice and liquid respectively, and ρ_{ice} is the density of solid ice. This equation is appropriate for Rayleigh scattering and is a commonly used diagnostic output for model evaluation.

Figure 18 presents the differences in the calculated process rates between the observed and parameterised PSDs. The results are presented as percentage errors, except for radar reflectivity, where the fractional difference is expressed as a difference in dB units. Positive differences mean that the parameterised distribution predicts a higher value than the observed distribution, and vice versa. As in Figures 8, 9, and 10, the time scale bars in each panel represent two minutes in each run.

We see that the performance varies greatly across the runs, but a common feature is the evidence that the sign of the fractional change in these calculated rates is directly related to the width of the parameterised PSD compared with the observed PSD. In Figure 10, we find that the parameterised PSD in R1–R6 is generally slightly broader than that observed, which corresponds to vapour growth rates that are underestimated, whilst the other processes calculated are overestimated. There is a notable exception in R4, where the parameterised PSD is slightly narrower than that observed (this segment, S3, is examined in more detail in Section 4.2.1). Interestingly, this segment corresponds to very well matching process rates with comparatively small errors. In R8–R11, where the parameterised PSD is generally narrower than the observed PSD, we see that the vapour growth rate is overestimated whilst the other processes calculated are underestimated.

The magnitude of errors also varies significantly with temperature. In R1–R6, we see that precipitation and vapour growth rates are well predicted, with errors generally less than ±10%. As discussed in Section 4.1.1, these runs are largely homogenous in nature, which leads to accurate parameterisations of the PSDs in these microphysical regimes, as seen in Figure 10. However, it is clear that the errors associated with aggregation rates at these temperatures are much higher, often exceeding 100%. Aggregation rates are strongly temperature dependent and are inefficient at low temperatures. Percentage errors of 100% correspond to a doubling in aggregation rate, which is significant at these low temperatures; this has the potential to have notable impacts on model microphysics evolution. The radar reflectivity has errors of up to ±2.5 dBZ, which may be a result of the narrow PSDs observed at these temperatures.

In R7 and R8, it is clear that there are large differences between the process rates and moments calculated using the observed PSD and parameterised PSDs. There are relative errors of up to 80% in vapour growth rate and −50% in precipitation rate. Aggregation rate is also poorly predicted, with errors up to −75%. Reflectivity has errors of more than −10 dBZ. As discussed in Section 4.1.2, these runs are microphysically complex with multiple particle populations and a range of particle habits. As a result, PSDs are poorly parameterised in these conditions and do not capture the range of particle sizes accurately, therefore we are lacking information about the concentration of large particles. This explains why reflectivity and aggregation rate, in particular, are highly inaccurate, as these processes are strongly influenced by the larger ice particles.

In R9–R11, we see errors of up to −25% in precipitation rates, up to 25% in vapour growth rates, and up to −50% in aggregation rates. In R9, CASIM underestimates reflectivity by 5–10 dBZ. In R10, we see that CASIM underestimates reflectivity by more than 5 dBZ in some parts of the run. In R11, the reflectivity is underestimated by up to 10 dBZ. These inaccuracies come from the high concentrations of small particles in these runs, as discussed in Section 4.1.3. As in R7 and R8, the parameterised PSD is strongly weighted towards the zeroth moment (particle concentration), which is dominated by the smallest particle sizes. This means there is no representation of the concentration of larger particles in the parameterised PSD, introducing significant errors into these process rates, which are dependent on higher moments.

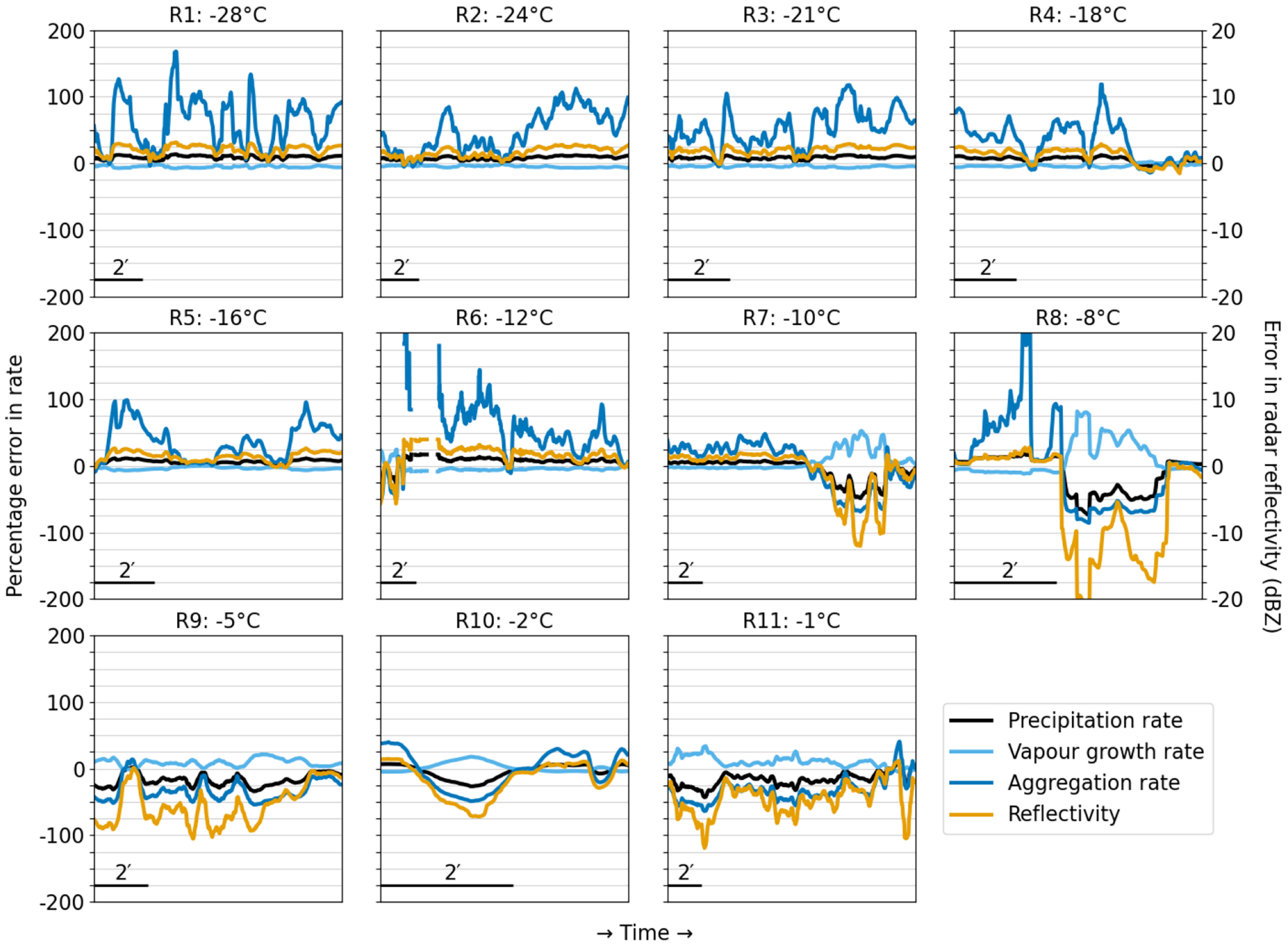

FIGURE 18 Percentage errors between precipitation rate, vapour growth rate and aggregation rate, and errors in radar reflectivity calculated from the observed PSD and the parameterised PSD. Note the differences in scale between the percentage errors and dB errors. Panel labels correspond to the runs described in Table 2. Time scale bars representing two minutes of each run are shown in each panel. [Colour figure can be viewed at wileyonlinelibrary.com]

5 | SUMMARY AND CONCLUSIONS

We have used our case study to analyse PSDs at different temperatures in a midlatitude frontal cloud, and have compared these with a gamma distribution from a double moment microphysics scheme using known shape parameters and observed moments. The gamma distribution used in this study matches that used in the UK Met Office's double moment microphysics scheme CASIM, but our findings would be relevant to many other double-moment microphysics schemes. Using this distribution, we have analysed whether a gamma distribution can represent the observed PSDs accurately with equal n and IWC. In our case study, we generally see the narrowest PSDs in low temperature/high altitude regions, with particle sizes remaining less than 3 mm. PSDs at these temperatures are generally captured relatively well by the parameterised distribution. This is because of the dominance of polycrystals at these temperatures and near homogeneity of the observed particle habit, which we see from the calculated area ratios of particles, implying similar growth histories for all particles. Consequently, the calculated vapour growth rate, precipitation rate, and radar reflectivity are reasonably accurate. The aggregation rate, however, is misrepresented by a factor of two, which illustrates the sensitivity of microphysical process rates to errors in the PSD.

At higher temperatures/lower altitudes, there is a broader range of particle sizes observed, with more varied particle habits and growth histories, including dendrites, needles, polycrystals, and aggregates. We see bimodal distributions resulting from the coexistence of distinct populations of particles and present evidence that some of these secondary populations are caused by SIP mixed with precipitation from higher cloud layers. We find that a gamma distribution is not sufficient to represent these complex microphysical cloud regions accurately. This inaccurate representation feeds through to the process rates and microphysical properties of the cloud; errors in the aggregation rate are in excess of 100% at times, while the radar reflectivities are frequently in error by several dB.

In many models (e.g., Field *et al.*, 2023), unrimed ice particles are split into two categories: cloud ice and snow, representing small and large particles. The action of primary nucleation and SIP in such models is to introduce more particles into the cloud ice category, some of which are gradually converted to snow. Each category has its own parameterised PSD, which is independent. Our findings suggest that when new particles are generated in a cloud they evolve into larger particles, which have distinct properties compared with the rest of the snow particles in the cloud; thus ice nucleation and SIP affect not only the generation rate of cloud ice but also the PSD of the snow category. One way to capture this could be to allow multiple unrimed snow particle types within the scheme, with the nucleation and subsequent evolution of each category acting independently, each contributing to the overall snow particle size distribution.

The data presented here constitute a single case study. What is not yet clear is how frequent bimodal populations such as those analysed in this study are in frontal clouds, or indeed within other cloud types. We are currently using radar Doppler spectra to investigate the occurrence of this multimodal behaviour across a large sample of clouds.

ACKNOWLEDGEMENTS

We acknowledge the efforts of Chris Walden and the staff at the Chilbolton Observatory in the collection of the radar data presented here. The aircraft measurements were made possible by the hard work of the staff at FAAM, and we are grateful to Emilia Sephton for operation of the Manchester cloud physics probes, and to Seb O'Shea, Richard Cotton, James Dorsey, and Freya Lumb for their work as Mission Scientists and instrument operators on the flight. The data collection was supported by NERC grant NE/P012426/1.

CONFLICT OF INTEREST STATEMENT

The authors declare no conflict of interest.

DATA AVAILABILITY STATEMENT

Data from the PICASSO field campaign are available through the CEDA Archive. Further information about the data and conditions for access are available at: https://www.ceda.ac.uk/services/ceda-archive/.

ORCID

Rosie M. Mammatt https://orcid.org/0009-0003-9712-6151

REFERENCES

Bailey, M.P. & Hallett, J. (2009) A comprehensive habit diagram for atmospheric ice crystals: confirmation from the laboratory, AIRS II, and other field studies. *Journal of the Atmospheric Sciences*, 66, 2888–2899. Available from: https://journals.ametsoc.org/view/journals/atsc/66/9/2009jas2883.1.xml

Baumgardner, D., Abel, S.J., Axisa, D., Cotton, R., Crosier, J., Field, P. et al. (2017) Cloud ice properties: in situ measurement challenges. *Meteorological Monographs*, 58, 9.1–9.23. Available from: https://journals.ametsoc.org/view/journals/amsm/58/1/amsmonographs-d-16-0011.1.xml

Baumgardner, D., Jonsson, H., Dawson, W., O'Connor, D. & Newton, R. (2001) The cloud, aerosol and precipitation spectrometer: a new instrument for cloud investigations. *Atmospheric Research*, 59-60, 251–264. Available from: https://www.sciencedirect.com/science/article/pii/S0169809501001193

Billault-Roux, A.-C., Georgakaki, P., Gehring, J., Jaffeux, L., Schwarzenboeck, A., Coutris, P. et al. (2023a) Distinct secondary ice production processes observed in radar Doppler spectra: insights from a case study. *Atmospheric Chemistry and Physics*, 23, 10207–10234. Available from: https://acp.copernicus.org/articles/23/10207/2023/

Billault-Roux, A.-C., Ghiggi, G., Jaffeux, L., Martini, A., Viltard, N. & Berne, A. (2023b) Dual-frequency spectral radar retrieval of snowfall microphysics: a physics-driven deep-learning approach. *Atmospheric Measurement Techniques*, 16, 911–940. Available from: https://amt.copernicus.org/articles/16/911/2023/

Brown, P.R.A. & Francis, P.N. (1995) Improved measurements of the ice water content in cirrus using a total-water probe. *Journal of Atmospheric and Oceanic Technology*, 12, 410–414. Available from: https://journals.ametsoc.org/view/journals/atot/12/2/1520-0426_1995_012_0410_imotiw_2_0_co_2.xml

Bryan, G.H. & Morrison, H. (2012) Sensitivity of a simulated squall line to horizontal resolution and parameterization of microphysics. *Monthly Weather Review*, 140, 202–225. Available from: https://journals.ametsoc.org/view/journals/mwre/140/1/mwr-d-11-00046.1.xml

Connolly, P.J., Emersic, C. & Field, P.R. (2012) A laboratory investigation into the aggregation efficiency of small ice crystals. *Atmospheric Chemistry and Physics*, 12, 2055–2076. Available from: https://acp.copernicus.org/articles/12/2055/2012/

Cotton, R.J., Field, P.R., Ulanowski, Z., Kaye, P.H., Hirst, E., Greenaway, R.S. et al. (2013) The effective density of small ice particles obtained from in situ aircraft observations of mid-latitude cirrus. *Quarterly Journal of the Royal Meteorological Society*, 139, 1923–1934. Available from: https://doi.org/10.1002/qj.2058

Crosier, J., Bower, K.N., Choularton, T.W., Westbrook, C.D., Connolly, P.J., Cui, Z.Q. et al. (2011) Observations of ice multiplication in a weakly convective cell embedded in supercooled mid-level stratus. *Atmospheric Chemistry and Physics*, 11, 257–273. Available from: https://acp.copernicus.org/articles/11/257/2011/acp-11-257-2011.html

DeMott, P.J., Prenni, A.J., Liu, X., Kreidenweis, S.M., Petters, M.D., Twohy, C.H. et al. (2010) Predicting global atmospheric ice nuclei distributions and their impacts on climate. *Proceedings of the*

National Academy of Sciences, 107, 11217–11222. Available from: https://doi.org/10.1073/pnas.0910818107

Ferrier, B.S. (1994) A double-moment multiple-phase four-class bulk ice scheme. Part I: description. *Journal of the Atmospheric Sciences*, 51, 249–280. Available from: https://journals.ametsoc.org/view/journals/atsc/51/2/1520-0469_1994_051_0249_admmpf_2_0_co_2.xml

Field, P.R. & Heymsfield, A.J. (2015) Importance of snow to global precipitation. *Geophysical Research Letters*, 42, 9512–9520. Available from: https://doi.org/10.1002/2015GL065497

Field, P.R., Heymsfield, J., Bansemer, A. & Twohy, C.H. (2008) Determination of the combined ventilation factor and capacitance for ice crystal aggregates from airborne observations in a tropical anvil cloud. *Journal of the Atmospheric Sciences*, 65, 376–391.

Field, P.R., Hill, A., Shipway, B., Furtado, K., Wilkinson, J., Miltenberger, A. et al. (2023) Implementation of a double moment cloud microphysics scheme in the UK met office regional numerical weather prediction model. *Quarterly Journal of the Royal Meteorological Society*, 149, 703–739. Available from: https://doi.org/10.1002/qj.4414

Field, P.R., Lawson, R.P., Brown, P.R.A., Lloyd, G., Westbrook, C., Moisseev, D. et al. (2017) Secondary ice production: current state of the science and recommendations for the future. *Meteorological Monographs*, 58, 7.1–7.20.

Gunn, K.L.S. & Marshall, J.S. (1958) The distribution with size of aggregate snowflakes. *Journal of the Atmospheric Sciences*, 15, 452–461.

Hallett, J. & Mossop, S.C. (1974) Production of secondary ice particles during the riming process. *Nature*, 249, 26–28. Available from: https://www.nature.com/articles/249026a0

Heymsfield, A., Schmitt, C. & Bansemer, A. (2013) Ice cloud particle size distributions and pressure-dependent terminal velocities from in situ observations at temperatures from 0° to −86°C. *Journal of the Atmospheric Sciences*, 70, 4123–4154.

Heymsfield, A.J., Schmitt, C., Bansemer, A. & Twohy, C.H. (2010) Improved representation of ice particle masses based on observations in natural clouds. *Journal of the Atmospheric Sciences*, 67, 3303–3318.

Hogan, R.J., Francis, P.N., Flentje, H., Illingworth, A.J., Quante, M. & Pelon, J. (2003) Characteristics of mixed-phase clouds. I: Lidar, radar and aircraft observations from CLARE'98. *Quarterly Journal of the Royal Meteorological Society*, 129, 2089–2116. Available from: https://doi.org/10.1256/rj.01.208

Hueholt, D.M., Yuter, S.E. & Miller, M.A. (2022) Revisiting diagrams of ice growth environments. *Bulletin of the American Meteorological Society*, 103, E2584–E2603.

Illingworth, A.J., Hogan, R.J., O'Connor, E., Bouniol, D., Brooks, M.E., Delanoé, J. et al. (2007) Cloudnet: continuous evaluation of cloud profiles in seven operational models using ground-based observations. *Bulletin of the American Meteorological Society*, 88, 883–898. Available from: https://doi.org/10.1175/BAMS-88-6-883

Keinert, A., Spannagel, D., Leisner, T. & Kiselev, A. (2020) Secondary ice production upon freezing of freely falling drizzle droplets. *Journal of the Atmospheric Sciences*, 77, 2959–2967.

Keppas, S.C., Crosier, J., Choularton, T.W. & Bower, K.N. (2017) Ice lollies: An ice particle generated in supercooled conveyor belts. *Geophysical Research Letters*, 44, 5222–5230. Available from: https://doi.org/10.1002/2017GL073441

Khain, A.P., Beheng, K.D., Heymsfield, A., Korolev, A., Krichak, S.O., Levin, Z. et al. (2015) Representation of microphysical processes in cloud-resolving models: Spectral (bin) microphysics versus bulk parameterization. *Reviews of Geophysics*, 53, 247–322. Available from: https://doi.org/10.1002/2014RG000468

Kneifel, S., Kulie, M.S. & Bennartz, R. (2011) A triple-frequency approach to retrieve microphysical snowfall parameters. *Journal of Geophysical Research: Atmospheres*, 116, D11203. Available from: https://doi.org/10.1029/2010JD015430

Kneifel, S., von Lerber, A., Tiira, J., Moisseev, D., Kollias, P. & Leinonen, J. (2015) Observed relations between snowfall microphysics and triple-frequency radar measurements. *Journal of Geophysical Research: Atmospheres*, 120, 6034–6055. Available from: https://doi.org/10.1002/2015JD023156

Korolev, A. & Leisner, T. (2020) Review of experimental studies of secondary ice production. *Atmospheric Chemistry and Physics*, 20, 11767–11797. Available from: https://acp.copernicus.org/articles/20/11767/2020/

Lance, S., Brock, C.A., Rogers, D. & Gordon, J.A. (2010) Water droplet calibration of the Cloud Droplet Probe (CDP) and in-flight performance in liquid, ice and mixed-phase clouds during ARCPAC. *Atmospheric Measurement Techniques*, 3, 1683–1706.

Lauber, A., Henneberger, J., Mignani, C., Ramelli, F., Pasquier, J.T., Wieder, J. et al. (2021) Continuous secondary-ice production initiated by updrafts through the melting layer in mountainous regions. *Atmospheric Chemistry and Physics*, 21, 3855–3870. Available from: https://acp.copernicus.org/articles/21/3855/2021/

Lauber, A., Kiselev, A., Pander, T., Handmann, P. & Leisner, T. (2018) Secondary ice formation during freezing of levitated droplets. *Journal of the Atmospheric Sciences*, 75, 2815–2826.

Lawson, R.P., Baker, B.A., Schmitt, C.G. & Jensen, T.L. (2001) An overview of microphysical properties of arctic clouds observed in May and July 1998 during FIRE ACE. *Journal of Geophysical Research: Atmospheres*, 106, 14989–15014. Available from: https://doi.org/10.1029/2000JD900789

Lawson, R.P., O'Connor, D., Zmarzly, P., Weaver, K., Baker, B., Mo, Q. et al. (2006) The 2D-S (Stereo) probe: design and preliminary tests of a new airborne, high-speed, high-resolution particle imaging probe. *Journal of Atmospheric and Oceanic Technology*, 23, 1462–1477. Available from: https://journals.ametsoc.org/view/journals/atot/23/11/jtech1927_1.xml

Lawson, R.P., Stewart, R.E. & Angus, L.J. (1998) Observations and numerical simulations of the origin and development of very large snowflakes. *Journal of the Atmospheric Sciences*, 55, 3209–3229.

Lean, H.W., Clark, P.A., Dixon, M., Roberts, N.M., Fitch, A., Forbes, R. et al. (2008) Characteristics of high-resolution versions of the met office unified model for forecasting convection over the United Kingdom. *Monthly Weather Review*, 136, 3408–3424.

Libbrecht, K.G. (2005) The physics of snow crystals. *Reports on Progress in Physics*, 68, 855. Available from: https://doi.org/10.1088/0034-4885/68/4/R03

Lin, Y.-L., Farley, R.D. & Orville, H.D. (1983) Bulk parameterization of the snow field in a cloud model. *Journal of Climate and Applied Meteorology*, 22, 1065–1092. Available from: https://journals.ametsoc.org/view/journals/apme/22/6/1520-0450_1983_022_1065_bpotsf_2_0_co_2.xml

Lloyd, G., Choularton, T., Bower, K., Crosier, J., Gallagher, M., Flynn, M. et al. (2020) Small ice particles at slightly supercooled temperatures in tropical maritime convection. *Atmospheric Chemistry and Physics*, 20, 3895–3904. Available from: https://acp.copernicus.org/articles/20/3895/2020/

Lloyd, G., Dearden, C., Choularton, T.W., Crosier, J. & Bower, K.N. (2014) Observations of the origin and distribution of ice in cold, warm, and occluded frontal systems during the DIAMET campaign. *Monthly Weather Review*, 142, 4230–4255.

Locatelli, J.D. & Hobbs, P.V. (1974) Fall speeds and masses of solid precipitation particles. *Journal of Geophysical Research (1896–1977)*, 79, 2185–2197. Available from: https://doi.org/10.1029/JC079i015p02185

Lohmann, U. & Feichter, J. (2005) Global indirect aerosol effects: a review. *Atmospheric Chemistry and Physics*, 5, 715–737. Available from: https://acp.copernicus.org/articles/5/715/2005/acp-5-715-2005.html

Lohmann, U., Stier, P., Hoose, C., Ferrachat, S., Kloster, S., Roeckner, E. et al. (2007) Cloud microphysics and aerosol indirect effects in the global climate model ECHAM5-HAM. *Atmospheric Chemistry and Physics*, 7, 3425–3446. Available from: https://acp.copernicus.org/articles/7/3425/2007/acp-7-3425-2007.html

Marshall, J.S. & Palmer, W.M.K. (1948) The distribution of raindrops with size. *Journal of Meteorology*, 5, 165–166. Available from: https://journals.ametsoc.org/view/journals/atsc/5/4/1520-0469_1948_005_0165_tdorws_2_0_co_2.xml

Milbrandt, J.A. & McTaggart-Cowan, R. (2010) Sedimentation-Induced Errors in Bulk Microphysics Schemes. *Journal of the Atmospheric Sciences*, 67, 3931–3948. Available from: https://journals.ametsoc.org/view/journals/atsc/67/12/2010jas3541.1.xml

Milbrandt, J.A. & Yau, M.K. (2005) A multimoment bulk microphysics parameterization. Part I: analysis of the role of the spectral shape parameter. *Journal of the Atmospheric Sciences*, 62, 3051–3064. Available from: https://journals.ametsoc.org/view/journals/atsc/62/9/jas3534.1.xml

Morrison, H. & Gettelman, A. (2008) A new two-moment bulk stratiform cloud microphysics scheme in the community atmosphere model, version 3 (CAM3). Part I: description and numerical tests. *Journal of Climate*, 21, 3642–3659. Available from: https://journals.ametsoc.org/view/journals/clim/21/15/2008jcli2105.1.xml

Mossop, S.C., Cottis, R.E. & Bartlett, B.M. (1972) Ice crystal concentrations in cumulus and stratocumulus clouds. *Quarterly Journal of the Royal Meteorological Society*, 98, 105–123. Available from: https://doi.org/10.1002/qj.49709841509

Mülmenstädt, J., Salzmann, M., Kay, J.E., Zelinka, M.D., Ma, P.-L., Nam, C. et al. (2021) An underestimated negative cloud feedback from cloud lifetime changes. *Nature Climate Change*, 11, 508–513. Available from: https://www.nature.com/articles/s41558-021-01038-1

Norbury, J.R. & White, W.J. (1971) A rapid-response rain gauge. *Journal of Physics E: Scientific Instruments*, 4, 601. Available from: https://doi.org/10.1088/0022-3735/4/8/013

Pasquier, J.T., Henneberger, J., Korolev, A., Ramelli, F., Wieder, J., Lauber, A. et al. (2023) Understanding the History of Two Complex Ice Crystal Habits Deduced From a Holographic Imager. *Geophysical Research Letters*, 50, e2022GL100247. Available from: https://doi.org/10.1029/2022GL100247

Phillips, V.T.J., Patade, S., Gutierrez, J. & Bansemer, A. (2018) Secondary ice production by fragmentation of freezing drops: formulation and theory. *Journal of the Atmospheric Sciences*, 75, 3031–3070. Available from: https://journals.ametsoc.org/view/journals/atsc/75/9/jas-d-17-0190.1.xml

Phillips, V.T.J., Yano, J.-I. & Khain, A. (2017) Ice Multiplication by Breakup in Ice-Ice Collisions. Part I: Theoretical Formulation. *Journal of the Atmospheric Sciences*, 74, 1705–1719. Available from: https://journals.ametsoc.org/view/journals/atsc/74/6/jas-d-16-0224.1.xml

Pruppacher, H.R. & Klett, J.D. (1997) *Microphysics of clouds and precipitation*. Atmospheric and oceanographic sciences library; v. 18. Dordrecht, 2nd edition. Dordrecht, the Netherlands: Kluwer Academic Publishers.

Rasch, P. & Carslaw, K. (2022) Aerosol-climate modeling. In: *Aerosols and climate*. Amsterdam, the Netherlands: Elsevier, pp. 187–248.

Reisner, J., Rasmussen, R.M. & Bruintjes, R.T. (1998) Explicit forecasting of supercooled liquid water in winter storms using the MM5 mesoscale model. *Quarterly Journal of the Royal Meteorological Society*, 124, 1071–1107. Available from: https://doi.org/10.1002/qj.49712454804

Seidel, J.S., Kiselev, A.A., Keinert, A., Stratmann, F., Leisner, T. & Hartmann, S. (2024) Secondary ice production - no evidence of efficient rime-splintering mechanism. *Atmospheric Chemistry and Physics*, 24, 5247–5263. Available from: https://acp.copernicus.org/articles/24/5247/2024/

Sekhon, R.S. & Srivastava, R.C. (1970) Snow Size Spectra and Radar Reflectivity. *Journal of the Atmospheric Sciences*, 27, 299–307. Available from: https://journals.ametsoc.org/view/journals/atsc/27/2/1520-0469_1970_027_0299_sssarr_2_0_co_2.xml

Senior, C.A. & Mitchell, J.F.B. (1993) Carbon dioxide and climate. the impact of cloud parameterization. *Journal of Climate*, 6, 393–418. Available from: https://journals.ametsoc.org/view/journals/clim/6/3/1520-0442_1993_006_0393_cdacti_2_0_co_2.xml

Sherwood, S.C., Webb, M.J., Annan, J.D., Armour, K.C., Forster, P.M., Hargreaves, J.C. et al. (2020) An assessment of earth's climate sensitivity using multiple lines of evidence. *Reviews of Geophysics*, 58, e2019RG000678. Available from: https://doi.org/10.1029/2019RG000678

Takahashi, T., Endoh, T., Wakahama, G. & Fukuta, N. (1991) Vapor diffusional growth of free-falling snow crystals between −3 and −23 ∘C. *Journal of the Meteorological Society of Japan. Ser. II*, 69, 15–30.

Taylor, J.W., Choularton, T.W., Blyth, A.M., Liu, Z., Bower, K.N., Crosier, J. et al. (2016) Observations of cloud microphysics and ice formation during COPE. *Atmospheric Chemistry and Physics*, 16, 799–826. Available from: https://acp.copernicus.org/articles/16/799/2016/acp-16-799-2016.html

Vardiman, L. (1978) The generation of secondary ice particles in clouds by crystal-crystal collision. *Journal of the Atmospheric Sciences*, 35, 2168–2180. Available from: https://journals.ametsoc.org/view/journals/atsc/35/11/1520-0469_1978_035_2168_tgosip_2_0_co_2.xml

von Terzi, L., Dias Neto, J., Ori, D., Myagkov, A. & Kneifel, S. (2022) Ice microphysical processes in the dendritic growth layer: a statistical analysis combining multi-frequency and polarimetric Doppler cloud radar observations. *Atmospheric Chemistry and Physics*, 22, 11795–11821. Available from: https://acp.copernicus.org/articles/22/11795/2022/

Wang, Y., Su, H., Jiang, J.H., Xu, F. & Yung, Y.L. (2020) Impact of Cloud Ice Particle Size Uncertainty in a Climate Model and Implications for Future Satellite Missions. *Journal of Geophysical Research-Atmospheres*, 125, e2019JD032119. Available from: https://doi.org/10.1029/2019JD032119

Wilson, D.R. & Ballard, S.P. (1999) A microphysically based precipitation scheme for the UK meteorological office unified model. *Quarterly Journal of the Royal Meteorological Society*, 125, 1607–1636. Available from: https://doi.org/10.1002/qj.49712555707

Wood, N.B., L'Ecuyer, T.S., Bliven, F.L. & Stephens, G.L. (2013) Characterization of video disdrometer uncertainties and impacts on estimates of snowfall rate and radar reflectivity. *Atmospheric Measurement Techniques*, 6, 3635–3648.

Wood, N.B., L'Ecuyer, T.S., Heymsfield, A.J., Stephens, G.L., Hudak, D.R. & Rodriguez, P. (2014) Estimating snow microphysical properties using collocated multisensor observations. *Journal of Geophysical Research-Atmospheres*, 119, 8941–8961. Available from: https://doi.org/10.1002/2013JD021303

Yano, J.-I. & Phillips, V.T.J. (2011) Ice-ice collisions: an ice multiplication process in atmospheric clouds. *Journal of the Atmospheric Sciences*, 68, 322–333.

Zhang, W., Shi, X. & Lu, C. (2022) Impacts of the ice-particle size distribution shape parameter on climate simulations with the Community Atmosphere Model Version 6 (CAM6). *Geoscientific Model Development*, 15, 7751–7766.

How to cite this article: Mammatt, R.M., Westbrook, C.D., Crosier, J. & McCusker, K. (2026) Evaluating the realism of double moment parameterised particle size distributions in a midlatitude frontal ice cloud with complex microphysics. *Quarterly Journal of the Royal Meteorological Society*, e70172. Available from: https://doi.org/10.1002/qj.70172